

*promoting access to White Rose research papers*



**Universities of Leeds, Sheffield and York**  
**<http://eprints.whiterose.ac.uk/>**

---

This is an author produced version of a paper published in **Journal of Chemical Physics**.

White Rose Research Online URL for this paper:  
<http://eprints.whiterose.ac.uk/4931/>

---

**Published paper**

Wilkinson, I. and Whitaker, B.J. (2008) *Photodissociation of NO<sub>2</sub> in the (2)B-2(2) state: A slice imaging study and reinterpretation of previous results*, Journal of Chemical Physics, Volume 129 (5),154312.

---

# Photodissociation of NO<sub>2</sub> in the (2)<sup>2</sup>B<sub>2</sub> state: A slice imaging study and reinterpretation of previous results

Iain Wilkinson and Benjamin J Whitaker\*

School of Chemistry  
University of Leeds  
Leeds LS2 9JT, UK

## Abstract

The photodissociation dynamics of nitrogen dioxide have been probed above the second dissociation limit at photolysis wavelengths close to 226 nm. The O(<sup>3</sup>P<sub>J</sub>) + NO(<sup>2</sup>Π<sub>Ω</sub>) product channel has been examined using direct current slice velocity map imaging of the O(<sup>3</sup>P<sub>J</sub>) and NO(<sup>2</sup>Π<sub>Ω</sub>) fragments. Mass-resolved REMPI spectroscopy and velocity map imaging have been used to probe directly the rovibrational population distributions of the NO fragments. We also examine possible interference from the dissociation of N<sub>2</sub>O<sub>4</sub> by investigating the effect of the sample temperature on the O(<sup>3</sup>P<sub>J</sub>) fragment energy distributions. The O(<sup>3</sup>P<sub>J</sub>) + NO(<sup>2</sup>Π<sub>Ω</sub>) dissociation channel has been found to favor the production of vibrationally cold, highly rotationally excited NO(<sup>2</sup>Π<sub>Ω</sub>) products with all three oxygen spin-orbit components. Other minor dissociation channels which produce O(<sup>3</sup>P<sub>J</sub>) atoms have also been identified. We discuss the significance of these dissociation channels and present a reinterpretation of previous studies of NO<sub>2</sub> dissociation on excitation to the (2)<sup>2</sup>B<sub>2</sub> state.

PACS: 33.15, 33.20, 37.20

Word count: 12882

Figs: 6

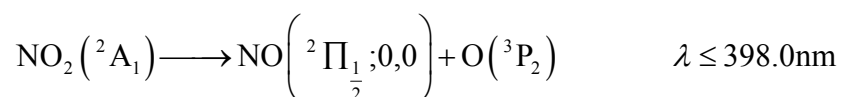
Keywords: DC slice velocity map imaging, NO<sub>2</sub> second dissociation limit, photodissociation

\* corresponding author

# I. Introduction

The photodissociation of nitrogen dioxide (NO<sub>2</sub>) has been studied for more than half a century. The molecule has received considerable attention due to interest in fundamental questions about the nature of unimolecular decomposition dynamics and also because of its important roles in the chemistry of combustion<sup>1</sup>, the stratosphere<sup>2</sup> and the troposphere<sup>2</sup>. Further interest arises from the strongly vibronically coupled nature of its low lying electronic states and subsequent non-adiabatic dynamics, which provide a significant challenge to theory due to the molecule's open shell structure.<sup>3,4</sup> Nitrogen dioxide also provides an experimental opportunity to study non-radiative decay processes in the small molecule limit.<sup>5</sup>

The absorption spectrum of NO<sub>2</sub> displays two broad features between 200 and 700 nm.<sup>6-9</sup> The first band is associated with excitation from the ground (1)<sup>2</sup>A<sub>1</sub> state to both the (1)<sup>2</sup>B<sub>1</sub> and (1)<sup>2</sup>B<sub>2</sub> electronically excited states with the majority of the oscillator strength lying on the (1)<sup>2</sup>B<sub>2</sub> ← (1)<sup>2</sup>A<sub>1</sub> transition.<sup>10</sup> The complexity of the absorption spectrum between 700 and 250 nm is attributed to vibronic coupling of the excited (1)<sup>2</sup>B<sub>2</sub> state to the other energetically accessible electronic manifolds (the electronically excited (1)<sup>2</sup>B<sub>1</sub> and (1)<sup>2</sup>A<sub>2</sub> states and the (1)<sup>2</sup>A<sub>1</sub> ground state). Close to the peak of the first electronic absorption feature, the first dissociation limit is reached 3.115545(6) eV above the origin of the (1)<sup>2</sup>A<sub>1</sub> state.<sup>11</sup>



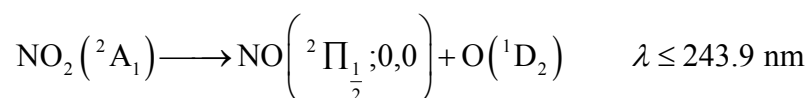
Higher energy excitation also produces NO in its <sup>2</sup>Π<sub>3/2</sub> spin-orbit state (14.856 meV above the NO(<sup>2</sup>Π<sub>1/2</sub>) ground state)<sup>12</sup> along with the production of NO in coincidence with O(<sup>3</sup>P<sub>1</sub>) and O(<sup>3</sup>P<sub>0</sub>) fragments (19.623 and 28.141 meV above the O(<sup>3</sup>P<sub>2</sub>) ground state respectively)<sup>13</sup>.

Since the original photofragment ion studies of Busch and Wilson in 1972,<sup>10,14</sup> the photodissociation of NO<sub>2</sub> via the (1)<sup>2</sup>B<sub>2</sub> state has been extensively studied. The literature is too extensive to review in any detail here. The rise of the second electronic absorption band of NO<sub>2</sub> is assigned to the opening of the (2)<sup>2</sup>B<sub>2</sub> ← (1)<sup>2</sup>A<sub>1</sub> transition at 4.97498 eV.<sup>15</sup> At these excitation energies the effect of the NO<sub>2</sub>/N<sub>2</sub>O<sub>4</sub>

equilibrium becomes important. Below 250 nm, the absorption cross-section of N<sub>2</sub>O<sub>4</sub> rises sharply, with the N<sub>2</sub>O<sub>4</sub> to NO<sub>2</sub> absorption cross-section ratio increasing from 0.01 at 400 nm to 100 close to 200 nm.<sup>7,9</sup> The ultraviolet photolysis of N<sub>2</sub>O<sub>4</sub> has been noted to produce electronically and vibrationally excited NO<sub>2</sub> as well as NO(<sup>2</sup>Π<sub>Ω</sub>) and O(<sup>3</sup>P<sub>J</sub>) products, making it difficult to separate the decomposition product channels of the two species.<sup>16-18</sup> The equilibrium results in ~81 % of NO<sub>2</sub> existing in its dimeric form at room temperature and atmospheric pressure (STP). The obvious implication of this is that photodissociation studies at wavelengths below 250 nm require careful reagent preparation, N<sub>2</sub>O<sub>4</sub> correction factors and/or experimental methods which allow the NO<sub>2</sub> and N<sub>2</sub>O<sub>4</sub> photoproducts to be distinguished.

The second electronic absorption band of NO<sub>2</sub> shows a much simpler vibronic structure than the visible/near UV band and was partially analyzed by Harris and King<sup>19</sup>. The symmetry of the excited state was later assigned as <sup>2</sup>B<sub>2</sub> when the band was further studied by Ritchie *et al.*<sup>20</sup> The transition corresponds to a linear superposition of the 5a<sub>1</sub>←3b<sub>2</sub> and 2b<sub>1</sub>←1a<sub>2</sub> valence electron excitations and carries an average oscillator strength of 0.0068 eV<sup>-1</sup>.<sup>9,21-23</sup> At its origin the (2)<sup>2</sup>B<sub>2</sub> state is known to be predissociative with a lifetime of 42 ± 5 ps.<sup>24</sup> The (2)<sup>2</sup>B<sub>2</sub> state is calculated to be weakly bound with a shallow potential well in the asymmetric stretching coordinate in the adiabatic representation.<sup>4</sup> For an overview of the topography of the (2)<sup>2</sup>B<sub>2</sub> surface and other relevant electronic states, the recent results of Schinke and co-workers are recommended.<sup>4</sup>

At higher excitation energies, 5.082909 eV, dissociation to produce NO in coincidence with electronically excited oxygen can occur,<sup>11,13</sup>



The O(<sup>1</sup>D<sub>2</sub>) yield is found to remain relatively constant, between 40 and 50%, upon direct excitation to the (2)<sup>2</sup>B<sub>2</sub> state above this energetic threshold.<sup>24-28</sup> Although full dynamical calculations on accurate potential energy surfaces are required to understand the details of the branching ratio into the two channels<sup>4</sup>, the significant O(<sup>3</sup>P<sub>J</sub>) yield can be rationalized by the correlation of the (2)<sup>2</sup>B<sub>2</sub> manifold with the NO(<sup>2</sup>Π<sub>Ω</sub>) + O(<sup>3</sup>P<sub>J</sub>) dissociation channel via the asymmetric stretch in the adiabatic

representation. The  $O(^1D_2)$  yield is then explained by the proximity of the adiabatic  $(3)^2B_2$  surface which correlates with the  $NO(^2\Pi_\Omega) + O(^1D_2)$  dissociation channel along the asymmetric stretch coordinate. This view is supported by the experimental results of Tsuji *et al.*<sup>26</sup> and Uselman and Lee<sup>24</sup> who observed that asymmetric stretch excitation in the  $(2)^2B_2$  state promoted the predissociation and also dramatically increased the  $O(^1D_2)$  yield close to the  $(2)^2B_2$  origin. On excitation to the  $(2)^2B_2$  state with two vibrational quanta in the asymmetric stretch, the excited state lifetime is observed to decrease below 100 fs.<sup>24,26</sup> No further marked decrease in lifetime is observed at higher excitation energies throughout the rest of the vibrational manifold.

A number of experiments have been carried out to measure the energy partitioning of the dissociation over a range of excitation wavelengths. The spin-orbit branching ratios (uncorrected for degeneracy and line-strength factors) of the ground state oxygen photoproducts have been measured by Rubahn *et al.* close to 226 nm<sup>29</sup> who obtained  $O(^3P_2):O(^3P_1):O(^3P_0)$  branching ratios of 1.00:0.71:0.25, 1.00:0.68:0.27 and 1.00:0.50:0.17 in a thermal sample, a neat supersonic expansion and a seeded supersonic expansion of  $NO_2$  respectively using laser induced fluorescence (LIF). Miyawaki *et al.*<sup>30</sup> carried out similar measurements at 212.9 nm in a molecular beam and determined a branching ratio of 1.00:0.35:0.08, suggesting that there is a weak wavelength dependence to the measured  $O(^3P_J)$  distribution between 226 and 213 nm. It is noteworthy that for excitation wavelengths longer than the  $(2)^2B_2$  band origin, that is to the continuum of the  $(1)^2B_2$  potential energy surface, both groups recorded similar spin-orbit ratios.

The production of  $NO(^2\Pi_\Omega)$  in coincidence with  $O(^3P_J)$  has been studied close to the  $(2)^2B_2$  origin, below the  $O(^1D_2)$  threshold, by a number of researchers. McKendrick *et al.*<sup>31</sup> measured NO fragments in both  $v = 2$  and 6 at a photolysis wavelength of 248.5 nm. Slanger *et al.*<sup>32</sup> later repeated this experiment but probing other vibrational levels ( $v = 4-8$ ) with a separate probe laser using LIF. They observed a marked vibrational inversion with the population distribution peaking at  $v = 7$ . McFarlane *et al.*<sup>33</sup> used a resonantly enhanced multiphoton ionization (REMPI) detection scheme to probe the whole vibrational distribution at the same photolysis wavelength. These experiments observed a bimodal vibrational distribution peaking at  $v = 0$  with a subsidiary maximum at  $v = 5$  (although the peak at  $v = 0$  has been questioned in the literature<sup>34</sup>). Non-statistical NO fragment rotational profiles were

also observed. More recently, Morrell *et al.* carried out a further study at 248 nm using time-resolved Fourier transform infra-red (TR FTIR) spectroscopy to measure the NO fragment fluorescence in  $v = 2-8$ .<sup>35</sup> The measured vibrational distribution was in qualitative agreement with McFarlene *et al.*; peaking at  $v = 5$ .

At slightly higher excitation energies and above the threshold for  $O(^1D_2)$  production the  $O(^3P_J)$  product channel has been studied using the velocity map imaging (VMI) technique by Ahmed *et al.*<sup>34</sup> and separately by Brouard *et al.*<sup>16</sup> Ahmed and co-workers measured the kinetic energy distribution of the unaligned  $O(^3P_0)$  fragment in a single laser experiment at 226.23 nm. Here the  $O(^3P_0)$  distribution was interpreted to peak in coincidence with  $NO(^2\Pi_\Omega)$  fragments in  $v = 4$  or 5 with an average translational anisotropy parameter of 1.32. Additionally, images of the  $NO(^2\Pi_\Omega)$  fragments were recorded using REMPI to ionize the fragments via the  $A \leftarrow X$  (0,0), (1,1) and (2,2) transitions. It was determined that the rotational profiles of the NO produced in coincidence with  $O(^1D_2)$  and  $O(^3P_J)$  were markedly different.

The Brouard group imaged all three spin-orbit components of the ground state oxygen fragment in a single laser experiment close to 226 nm. The kinetic energy profiles of the oxygen fragments were found to be bimodal and to depend strongly on the partial pressure of the  $NO_2$  in the sample mixture. The signal strength of the slow component was found to be particularly sensitive to the  $NO_2$  partial pressure although the kinetic energy spread of the fast component was also observed to narrow as the  $NO_2$  partial pressure was reduced. The slow component was attributed to the dissociation of  $N_2O_4$  at 226 nm to produce  $NO_2$  with both NO and  $O(^3P_J)$ <sup>35,36</sup>. The broadening of the fast component was attributed to the photolysis of  $N_2O_4$  to produce translationally hot  $NO_2$  fragments<sup>18,37,38</sup> which were subsequently photolysed to produce  $O(^3P_J)$ . The  $O(^3P_J)$  images recorded at low  $NO_2$  partial pressures were ascribed to the photolysis of  $NO_2$  alone with the  $O(^3P_0)$  kinetic energy distribution obtained at low partial pressure being narrower than that measured by Ahmed *et al.* It was, therefore, suggested that the distribution obtained by Ahmed *et al.* contained interference from the photolysis of  $N_2O_4$  contaminant. Brouard *et al.* interpreted their low pressure data as being due to  $O(^3P_0)$  fragments produced in coincidence with  $NO(^2\Pi_\Omega)$  in  $v = 4-6$ . The translational anisotropy of the total  $O(^3P_0)$  distribution was determined to be  $\sim 1.0$ . The analysis of the  $O(^3P_2)$  and  $O(^3P_1)$  images may be affected by orbital angular momentum alignment effects and as a result the anisotropies of

these images were not published. Despite the efforts of the Brouard group to minimize the  $\text{N}_2\text{O}_4$  content of their supersonic expansion, the slow component of the signal is still dominant in their  $\text{O}(^3\text{P}_2)$  distribution.

At 212.8 nm the photodynamics of the dissociation have been studied by Ahmed *et al.*<sup>39</sup> and by Richter *et al.*<sup>40</sup> Ahmed *et al.* used VMI in order to measure the orbital angular momentum alignment of the  $\text{O}(^3\text{P}_2)$  and  $\text{O}(^3\text{P}_1)$  photofragments and also recorded images of the unaligned  $\text{O}(^3\text{P}_0)$  fragment. At this excitation energy, the alignment of the  $\text{O}(^3\text{P}_2)$  fragment was found to be negligible, in contrast, the  $\text{O}(^3\text{P}_1)$  fragment was found to display appreciable orbital alignment. The  $\text{O}(^3\text{P}_1)$  kinetic energy release spectrum displayed a bimodal distribution, peaking at a translational energy consistent with the co-production of  $\text{NO}(^2\Pi_\Omega)$  in  $v = 4$ . A subsidiary maximum at low kinetic energy was assigned to the production of  $\text{O}(^3\text{P}_1)$  in coincidence with  $\text{NO}(^2\Pi_\Omega)$  in  $v = 10$  or  $11$ . The spin-orbit branching ratios were noted to be markedly different for the fast and slow  $\text{O}(^3\text{P}_j)$  fragments. The time-of-flight mass spectrometry  $\text{O}(^3\text{P}_2)$  experiments of Richter *et al.* agree qualitatively with the measurements of Ahmed *et al.*, also suggesting a bimodal fragment distribution with a peak close to the energy associated with NO molecules in  $v = 4$ .

At higher excitation energies, Coriou *et al.* used the VMI technique to probe the  $\text{O}(^3\text{P}_j)$  fragment distribution close to 200 nm in a single laser experiment.<sup>41</sup> A bimodal velocity distribution was observed for all three spin-orbit components. In each case the distribution peaked at speeds consistent with the production of highly vibrationally excited NO fragments, in  $v = 13$  or  $14$ . A secondary peak was interpreted to be due to  $\text{NO}(^2\Pi_\Omega)$  in a vibrational level close to  $7$ . As with the results obtained at lower excitation energies, potential angular momentum alignment of the  $\text{O}(^3\text{P}_2)$  and  $\text{O}(^3\text{P}_1)$  may have effected the measured kinetic energy profiles and translational anisotropies. However the fast component of the unaligned  $\text{O}(^3\text{P}_0)$  fragment anisotropy was measured to be  $\sim 1.0$ , in accord with the results of Brouard *et al.* close to 226 nm. The anisotropy of the slow component was measured to be  $0.55$  implying dissociation taking place on a longer timescale and/or via a more bent geometry.

The time-resolved FTIR experiments of Hancock and Morrison at 193 nm also suggest a bimodal vibrational distribution of the  $\text{O}(^3\text{P}_j)$  fragments.<sup>25</sup> By recording the

fluorescence of the NO fragments produced in coincidence with both ground and electronically excited state oxygen atoms, the overall vibrational distribution was measured. The primary peak in the distribution occurs with NO in  $v = 5$ , which may be due to either the  $O(^3P_J)$  or  $O(^1D)$  dissociation channel. Above  $v = 6$ , NO can only be formed in coincidence with  $O(^3P_J)$  fragments. The vibrational populations between  $v = 7$  and 16 displayed bimodal structure, peaking at  $v = 7$  (and perhaps below with a contribution from the  $O(^1D_2)$  co-fragments) with an ancillary maximum at  $v = 14$ . An interesting aspect of these experiments is that their time-resolved nature should have identified any contributions from the dissociation of  $N_2O_4$ . The absence of these contributions seems to suggest that the  $O(^3P_J)$  dissociation is genuinely vibrationally bimodal; at least at 193 nm.

In summary, the literature regarding the energy partitioning in the dissociation of  $NO_2$  from the  $(2)^2B_2$  state does not paint an entirely consistent picture. At 248 nm, the  $O(^3P_J)$  distribution has been measured to peak with  $NO(^2\Pi_\Omega)$  in  $v = 0$  with a subsidiary maximum somewhere between  $v = 5$  and 7.<sup>31-33,35</sup> At 226 nm the distribution is interpreted as peaking somewhere between  $v = 4$  and 6.<sup>16,34</sup> At slightly higher excitation energies, 213 nm, a bimodal distribution is measured with a major peak at a kinetic energy consistent with the production of  $NO(^2\Pi_\Omega)$  fragments in  $v = 4$  with an ancillary maximum consistent with production in  $v = 10$  or 11<sup>39</sup>. Close to 200 nm, the kinetic energy of the  $O(^3P_J)$  fragments are consistent with production in coincidence with  $NO(^2\Pi_\Omega)$  in  $v = 7$  and  $v = 13$  or 14.<sup>41</sup> At still shorter wavelengths, the  $NO(^2\Pi_\Omega)$  distribution is found to peak at  $v = 7$  or less with a small peak at  $v = 14$  in the  $NO(^2\Pi_\Omega) + O(^3P_J)$  distribution.<sup>25</sup> The energy partitioning determined by all of these studies is summarized in Fig. 1. The most probable internal energy of the photofragments is plotted against the initial excess energy in the  $(2)^2B_2$  state for the high and low energy channels respectively. The “error bars” represent the half-width half-maxima of the reported internal energy profiles in each study. In the study of Hancock and Morrison<sup>25</sup> only a vibrational profile was reported (represented by open triangles in the figure). However the calculations of Schinke *et al.*<sup>4</sup> allow us to estimate the expected rotational energy in the low (internal) energy channel. Accordingly we have also reported Hancock and Morrison’s datum with an additional 695 meV of internal rotational energy (solid triangle).

The dissociation dynamics close to 226 nm are particularly interesting. This is the only excitation wavelength at which a bimodal  $O(^3P_J)$  energy distribution has been attributed to  $N_2O_4$  photolysis. The two imaging studies carried out close to this excitation wavelength measured  $O(^3P_J)$  distributions with similar profiles.<sup>16,34</sup> However, these studies differ substantially in the determined kinetic energies of the peaks of the  $O(^3P_J)$  fragment distributions. In this paper we describe experiments at photolysis wavelengths close to 226 nm using the direct current (DC) slice imaging detection technique.<sup>42</sup> We achieve substantially higher energy resolution of the  $O(^3P_J)$  kinetic energy release spectra than has been obtained previously. We couple these experiments with detection of the NO co-fragments in order to understand the energy partitioning of the dissociation and the mechanism in more detail. The results of these experiments allows us to reappraise critically previous observations and to provide a new interpretation of the photodissociation dynamics of the  $(2)^2B_2$  state of  $NO_2$  that is in accord with recent theoretical work.<sup>4</sup> The paper is organized in the conventional experimental, results, discussion format.

## II. Experimental

In our experiments DC slice velocity map imaging<sup>42</sup> has been employed in conjunction with mass resolved REMPI spectroscopy in order to probe the nitric oxide and atomic oxygen photoproducts of nitrogen dioxide photolysis close to 226 nm. Reagent molecules were prepared in a pulsed supersonic expansion of 2%  $NO_2$  (Air Products Ltd.) purified by reaction with 5%  $O_2$  (BOC gases) in a seed gas of He (BOC gases). The supersonic expansion was created by a heated pulsed valve (General Valve) with a 500  $\mu\text{m}$  orifice and a backing pressure of  $\sim 1$  bar. For all of the experiments other than the temperature studies, the nozzle was held at 393 K in order to push the  $NO_2/N_2O_4$  equilibrium to 99.9 % in favor of the monomer. The expansion chamber was held at a pressure between  $1-8 \times 10^{-6}$  mbar throughout the experiments. The rotational temperature of the molecular beam was determined to be  $\sim 20$  K from the rotational profile of NO contaminant in the  $NO_2$  expansion. This molecular beam was doubly skimmed 50 mm and 600 mm downstream from the orifice, using 1 mm and 2 mm diameter skimmers (Beam Dynamics) respectively, in order to limit its translational velocity perpendicular to the direction of travel. The second skimmer lies at the base of a set of VMI ion/electron optics based on the designs of Wrede<sup>43</sup> and Suzuki<sup>44</sup>. The electron optics were mounted so as to project the photoion or

photoelectron distributions along the axis of the molecular beam propagation and were designed to operate both in conventional VMI<sup>45</sup> and DC slicing modes<sup>42</sup> depending on the extraction voltages employed. The detection chamber was held at a pressure close to  $1 \times 10^{-8}$  mbar throughout these experiments.

The frequency tripled output of a Nd:YAG laser (Continuum Surelite III-10) was used to pump a dye laser (Sirah Cobra Stretch) operating with a Coumarin 2 (Exciton) and, separately, a Coumarin 47 dye (Exciton) to span the required excitation wavelengths. The fundamental was frequency doubled to produce pulses with maximum energies between 2.5 and 3 mJ pulses at a repetition rate of 10 Hz between 218 and 236 nm with a temporal profile of 3 ns (FWHM). During the experiments, the laser energy was maintained between 50 and 500  $\mu$ J and was focused 2 mm beyond the molecular beam jet with a 250 mm fused silica lens. The single laser pulse photodissociated and ionized the photofragments via (1+1) or (2+1) REMPI processes for the nitric oxide and oxygen fragments respectively.

Photoions/photoelectrons were detected at the end of a mu-metal time-of-flight (TOF) tube by a dual micro channel plate vacuum detector in a chevron arrangement (40 mm diameter, with a P43 phosphor screen; Photek). The detector was gated to detect ions of a given mass, and for slicing experiments to detect the central part of one of the photoproduct distributions. In the slicing experiments, the detector on-time was maintained below 20 ns (usually less than 10 ns) using a custom built power supply (Photek). Images were captured using a  $640 \times 480$  pixel charged couple device (CCD) camera (LaVision Imager 3) and were averaged and processed using the DaVis software package (LaVision) and an event counting macro. Conventional velocity map images were post-processed using the Hankel/Abel transform to reconstruct the photoproduct distributions after the projection.<sup>46</sup> The resulting velocity map images were calibrated using NO photoionisation or O<sub>2</sub> photodissociation, the mechanisms and energetics of which are well understood.

### III. Results

DC slice images of the three O(<sup>3</sup>P<sub>J</sub>) fragments were recorded using a single laser, scanning the Doppler profiles of the fragments in order to probe the entire distributions. In these experiments, the pulse energies were maintained close to

250  $\mu\text{J pulse}^{-1}$ . The resulting images are shown in Fig. 2 (panels a, b and c). The corresponding calibrated kinetic energy release spectra are shown in the same figure (panels d, e and f). The kinetic energy resolved spin-orbit branching ratio was determined in separate experiments in which the three images were recorded on the same day under identical conditions (nozzle temperature 393 K, backing pressure 1 bar). The relative signal intensity ratio of the  $\text{O}(^3\text{P}_j)$  fragments with kinetic energies between 0.50 and 1.55 eV was determined to be 1.00:0.71:0.15 for the  $\text{O}(^3\text{P}_2)$ ,  $\text{O}(^3\text{P}_1)$  and  $\text{O}(^3\text{P}_0)$  fragments respectively. The image intensities in Fig. 2 have been normalized to this ratio. This normalization allowed the spin-orbit intensity ratio of the slower fragments to be extracted. For the fragments with kinetic energies between 0 and 0.5 eV this was determined to be 1.00:0.47:0.11.

The kinetic energy distributions of the atomic oxygen fragments are highly structured. The  $\text{O}(^3\text{P}_1)$  and  $\text{O}(^3\text{P}_0)$  fragment distributions peak at kinetic energies of 1.03 and 1.04 eV respectively. The  $\text{O}(^3\text{P}_2)$  distribution shows two major peaks at 0.95 and 1.05 eV.

Further experiments were performed to probe the  $\text{NO}(1)^2\Pi_\Omega$  fragments directly. In these experiments, the NO fragments were probed state specifically via a (1+1) REMPI scheme on the  $\text{A}\leftarrow\text{X}(1^2\Pi_r^+\leftarrow 1^2\Pi_\Omega)$  transitions. These experiments probe the NO fragments produced in coincidence with  $\text{O}(^3\text{P}_j)$  and  $\text{O}(^1\text{D}_2)$  fragments since both product channels are open below 243.9 nm. Spectra were collected by recording the total mass-resolved (by time-of-flight)  $\text{NO}^+$  signal arriving at the phosphor screen while scanning the excitation/probe wavelength. The spectra of the (0,0), (1,1) and (2,2) bands so recorded were in good agreement with those obtained by Im and Bernstein<sup>47</sup> and Grant and co-workers<sup>48</sup>. Velocity map images recorded in these bands confirmed the observations of Ahmed *et al.* that the two product channels produce NO fragments with very different rotational profiles.<sup>34</sup> Furthermore, for all of the probed rotational lines in these bands, the  $\text{NO}(^2\Pi_\Omega)$  fragments produced in coincidence with  $\text{O}(^3\text{P}_j)$  are the minor photoproducts.

Mass-resolved REMPI spectra measured across the excitation region of the (2,3) band display very different rotational profiles to the (0,0), (1,1) and (2,2) bands. The REMPI profile of the NO fragments recorded close to the (2,3) band head is shown in Fig. 3 (a). A progression of peaks separated by  $\sim 4.6$  meV occurs for

excitation energies between 5.34 and 5.41 eV in good agreement with the results of Im and Bernstein.<sup>47</sup> Some representative velocity map ion images recorded in different rotational states corresponding to peaks (a), (b) and (c) in Fig. 3 (a) are shown in Fig. 4.

In order to measure the effect of N<sub>2</sub>O<sub>4</sub> on the O(<sup>3</sup>P<sub>J</sub>) kinetic energy distributions, O(<sup>3</sup>P<sub>J</sub>) images were recorded at 295, 345 and 393 K. The resulting energy distributions are shown in Fig. 5. A broad feature is observed in the O(<sup>3</sup>P<sub>2</sub>) distributions at low temperatures which becomes less significant as the temperature is increased to 393 K. This feature was found to be most significant in the O(<sup>3</sup>P<sub>2</sub>) distribution.

## IV. Discussion

### 1. O(<sup>3</sup>P<sub>J</sub>) spin-orbit branching ratios

The photofragment speed distributions and velocity anisotropy will be affected by orbital angular momentum alignment effects. In a one laser one color experiment it is impossible to quantify these effects, although the O(<sup>3</sup>P<sub>0</sub>) fragment is intrinsically unaligned. A qualitative measure of the orbital alignment in the other O(<sup>3</sup>P) channels may be obtained by recording images with the laser polarization oriented perpendicular to the face of the detector. Since the photoproduct distribution created in a single laser, single photon dissociation process must be azimuthally symmetric any anisotropy is direct evidence for alignment effects in the photoproduct distribution. From the isotropic profile of the O(<sup>3</sup>P<sub>2</sub>) fragments recorded with the laser polarized perpendicular to the detector we conclude that the O(<sup>3</sup>P<sub>2</sub>) products are essentially unaligned, at least for the faster more intense component. In contrast, the O(<sup>3</sup>P<sub>1</sub>) image in the perpendicular configuration displayed a significant anisotropy indicating at least some orbital alignment. These qualitative observations are consistent with those of Ahmed *et al.* who, in a two color experiment at a photolysis wavelength of 213 nm, were able to make quantitative measurements.<sup>39</sup>

Our basic alignment experiments, together with the results of Ahmed *et al.*, suggest that the fast component (0.5-1.55 eV) of the O(<sup>3</sup>P<sub>2</sub>) distribution (Fig. 3) is not significantly aligned. This means that the observed intensity ratio of the O(<sup>3</sup>P<sub>2</sub>) to O(<sup>3</sup>P<sub>0</sub>) images should give a good measure of the true spin-orbit branching ratio. In

contrast, because the  $O(^3P_1)$  photoproducts are most probably aligned their measured intensity must be considered as a lower bound. With this caveat, the spin-orbit intensity ratio of the fast  $O(^3P_J)$  fragments is determined to be 1.00:0.71:0.15 at a sample temperature of 393 K; in slight disagreement with the results of Rubahn *et al.*<sup>29</sup> Normalizing the ratio with respect to the two photon line strengths and the state degeneracies highlights the preference of the dissociation for the production of  $O(^3P_1)$  photoproducts, which is markedly non-statistical (in agreement with the results of Rubahn *et al.*<sup>29</sup>). The spin-orbit intensity ratio of the slow  $O(^3P_J)$  fragments (0-0.5 eV of kinetic energy) was found to be quite different; favoring dissociation to produce  $O(^3P_2)$  photoproducts. We obtain a branching ratio of 1.00:0.47:0.11 (uncorrected for degeneracy and line strength factors) at a sample temperature of 393 K, although the orbital angular momentum alignment effects mean that the  $O(^3P_1)$ , and possibly the  $O(^3P_2)$ , signals are lower bounds of the real intensities. Despite this, the difference in the spin-orbit branching ratio must reflect real differences in the dissociation dynamics of the slow and fast fragments.

## **2. Energy partitioning in the NO fragments**

Our single laser experiments were performed with varying excitation wavelengths between 232 and 220 nm in order to probe different photolysis products. The range of excitation wavelengths populates different vibrational levels of the  $(2)^2B_2$  state of the parent  $NO_2$  molecules. However, the vibrational structure of the absorption spectrum in this region is primarily associated with the bound symmetric stretch in the  $(2)^2B_2$  vibrational manifold. This stretch can be considered as orthogonal to the unbound, dissociative asymmetric stretch coordinate, and should have no appreciable effect on the  $O(^1D_2) / O(^3P_J)$  branching ratio or dissociation timescale. It should also be noted that due to the change in the photolysis wavelength required to Doppler scan over each  $O(^3P_J)$  ionization resonance, structure due to individual rotational levels in the NO co-fragment cannot be resolved in these single laser experiments. Despite this, the energy distributions of all three  $O(^3P_J)$  spin-orbit components are highly structured (Figs. 2 (d)-(f)).

Focusing on the intrinsically unaligned  $O(^3P_0)$  distribution (Fig. 2 (f)), the majority of the oxygen atoms are formed with kinetic energies between 1.55 and 0.50 eV. This part of the distribution can be split into at least seven distinct peaks

(labeled a-g). The maximum of the distribution occurs at a kinetic energy consistent with the production of  $O(^3P_0)$  in coincidence with  $NO(^2\Pi_{1/2})$  in  $v = 3$  and  $N \sim 21$ . This is in good agreement with the results of Ahmed *et al.*<sup>34</sup> when the vibrational comb in their paper is corrected so that  $v = 0$  is positioned at a total photofragment kinetic energy consistent with dissociation via the  $NO(^2\Pi_{1/2}) + O(^3P_0)$  limit ( $\sim 2.379$  eV). With the correction to the results of Ahmed *et al.*, the peak in their and our distributions are in slight disagreement with Brouard *et al.* who claim that the peak of the distribution is consistent with  $NO(^2\Pi_\Omega)$  production in  $v = 4-6$ . Considering the reported high kinetic energy peaks of the  $O(^3P_J)$  distributions observed at 248, 213 and 200 nm (consistent with maxima at  $v = 0$ ,  $v = 4$  and  $v = 7$ ) a distribution peaking at  $v = 3$  for a photolysis wavelength of 226 nm appears to be consistent with the majority of the previous results (see Fig. 1) and we conclude that the differences between the reported energy distributions must be due to errors in the calibration of the ion images.

If the  $O(^3P_J)$  fragments do peak at an energy consistent with the production of the  $NO(^2\Pi_\Omega)$  co-fragments in  $v = 3$  (as implied by the results of Ahmed *et al.*<sup>34</sup> and our work), the mass-resolved REMPI spectrum recorded for excitation energies between 5.41 and 5.34 eV (229 to 232 nm, see Fig. 3 (a)) should reveal the rotational profile of these fragments. Between 5.41 and 5.34 eV  $NO(^2\Pi_\Omega)$  fragments can only be produced in coincidence with  $O(^1D_2)$  in  $v = 0$  or 1. This means that the spectral signature of the  $v = 3$  fragments would be due to the  $O(^3P_J)$  dissociation channel only. Rotationally cold  $NO(^2\Pi_{1/2})$  in  $v = 3$  is expected to be observed at 5.3692 eV (230.92 nm) due to the reasonable transition probabilities for the  $A \leftarrow X$  (2,3) transition (see Table 1) and assumed large population of the  $NO(^2\Pi_\Omega)$   $v = 3$  level (based on the  $O(^3P_J)$  energy distributions). Given the  $NO(^2\Pi_\Omega)$  and  $NO(^2\Sigma^+)$  rotational constants ( $1.7049$   $\text{cm}^{-1}$  and  $1.9956$   $\text{cm}^{-1}$  respectively) and knowing the higher order terms in the Dunham expansion,<sup>12,49</sup> and the origin of the  $NO(^2\Sigma^+)$  A state at  $5.45105$   $\text{eV}$ <sup>12</sup>, intense peaks in the  $v = 3$  rotational profile would be expected to occur at an excitation energy  $\sim 5.3838$  eV (230.29 nm) with prominent rotational lines separated by  $\sim 1.5$  meV. Examination of the REMPI spectrum in Fig. 3 (a) reveals no such feature! Instead a broad rotational progression with average peak spacing of  $\sim 4.6$  meV is visible. Clearly the observed rotational profile does not originate at 5.3692 eV (the  $A \leftarrow X$  (2,3) band origin, shown as a dashed vertical line in the figure)

and the NO co-fragment associated with the peak of the  $O(^3P_0)$  kinetic energy release spectrum cannot be in  $v = 3$ . We confirm this remark by presenting a simulated absorption profile, obtained using the LIFBASE program<sup>50</sup>, of NO fragments in  $v = 3$  with a statistical rotational profile peaking at  $N \sim 21$  in Fig. 3 (b).

We have already noted that the recorded REMPI spectrum is in agreement with the spectrum observed by Im and Bernstein between 5.23 and 5.46 eV. They attributed the signal to a multiphoton dissociation process<sup>47</sup> but this is not our interpretation. Several representative single laser mass resolved velocity map images of the NO fragment recorded between 5.34 and 5.43 eV are shown in Fig. 4. These images have been recorded for the peaks marked a, b and c in the REMPI spectrum (Fig. 3 (a)). Analysis of the kinetic energies of these fragments indicates that if they were from NO in  $v = 3$ , the probed states would span rotational states between  $N = 18$  and  $N = 33$ . This would result in peak separations between 1.2 and 2.5 meV in the REMPI spectrum, which are not observed. Furthermore, comparison of the photolysis/probe wavelengths used to obtain the images with the  $NO(^2\Pi_\Omega) A \leftarrow X(2,3)$  absorption lines in LIFBASE<sup>50</sup> indicates that the NO fragments with 18-30 quanta of rotational energy could not be probed by the applied laser field. In order to produce a rotational profile with peak separations of the order of 4.6 meV fragments with significantly higher rotational energies are required, corresponding to NO fragments occupying rotational levels with quantum numbers around 57, or  $\sim 700$  meV of rotational excitation.

The requirement for rotational excitation in the 700 meV range and the kinetic energy release observed in Fig. 4 is only consistent with NO fragments in the vibrational range of  $v = 0$  to 2. Considering the ionization stage of the experiment, summing the photon energy and the maximum vibrational energy of the  $NO(^2\Pi_\Omega)$  fragments ( $v = 2$ ), an energy between 5.92 and 5.99 eV can be accessed over the excitation range of Fig. 3 (a) at the one photon level. This means that the  $NO(^2\Pi_\Omega)$  fragments could only be probed via the  $(1)^2\Sigma^+$  (A) or the  $(2)^2\Pi_\Omega$  (B) intermediate state (with term energies of 5.45105 and 5.69256 eV respectively)<sup>12</sup> in a (1+1) REMPI process. It is also noted that ionization of the NO B state is forbidden within a Koopmans' type picture of the (1+1) ionization process. This is consistent with experimental studies in which the NO B state fluorescence is observed without any competition from ionization. There are no intermediate resonances at the two photon

level for a (2+1) ionization process of the NO fragments. Therefore one must conclude that the carrier of the spectrum in Fig. 3 (a) must be NO  $(1)^2\Pi_\Omega$  (X state) fragments in  $v = 0, 1$  or  $2$  probed via a (1+1) REMPI process using the NO  $(1)^2\Pi_\Omega$  (A) state as an intermediate resonance.

Because of the shorter bond length of the NO A state with respect to the X state (106.37 and 115.08 pm respectively), the rotational bands of the  $A\leftarrow X$  transitions are shaded to the blue. We therefore expect the absorption lines of rotationally excited NO fragments which are probed via the A state to occur at higher excitation energies than the vibrational band head. With the constraints on the populated vibrational levels of the  $\text{NO}(^2\Pi_\Omega)$  fragments imposed by the energetics, there are only two vibrational bands which we may be probing in Figs. 3 (a) and 4; the (1,2) and (0,1) bands. The line spacing and line intensities observed in Fig. 3 (a) imply a rotational profile which peaks in a rotational level close to 57. For the  $A\leftarrow X$  transition, the 57<sup>th</sup> rotational level in the Q branch should occur  $\sim 113$  meV to the blue of the (1,2) and (0,1) band heads. Based on the information in Table 1, we expect the Q(57) rotational line of the (1,2) and (0,1) vibrational bands to occur at 5.425 and 5.368 eV respectively. We therefore attribute the spectrum shown in Fig. 3 (a) to highly rotationally excited NO  $(1)^2\Pi_\Omega$  fragments produced in  $v = 1$ .

The assignment is confirmed by comparison of Fig. 3 (a) with simulations of the NO  $^2\Pi_\Omega$   $A\leftarrow X$  absorption spectrum using LIFBASE as shown in Fig. 3 (c). The simulated line positions match the observed positions for  $\text{NO}(^2\Pi_\Omega)$  populations in  $v = 1$ . A non-statistical rotational distribution spanning  $N = 52$  to  $65$  and peaking close to  $N = 60$  simulates the intensity profile of the NO fragments; although exact agreement was not sought and is not expected since LIFBASE is only capable of simulating an absorption spectrum and not a REMPI spectrum. The rotational energies of the imaged NO fragments can be calculated from their kinetic energies assuming that the fragments have one quanta of vibrational excitation. The measured kinetic energies of the NO fragments (Fig. 4) are consistent with production in  $v = 1$  with rotational quantum numbers between 49 and 58.

In the light of this new rovibrational assignment, the  $\text{NO}(^2\Pi_\Omega)$  fragments probed by Im and Bernstein's experiment between 5.23 and 5.46 eV correspond to the entire rotational distribution of the  $A\leftarrow X$  (0,1) vibrational band.<sup>47</sup> Despite these

features being previously attributed to multiphoton dissociation of  $\text{NO}_2$ , the rotational profile they observed is exactly what is expected for a narrow, highly rotationally excited rotational profile of  $\text{NO}$  fragments produced in coincidence with  $\text{O}(^3\text{P}_J)$ . When REMPI spectra are recorded at either side of the spectrum shown in Fig. 3 (a), we find that the peak of the rotational distribution occurs close to 231 nm. If one considers the transition probabilities (see Table 1) of the vibrational bands close to the studied wavelengths, one sees that the transition probability for the  $\text{A}\leftarrow\text{X}$  (0,1) transition is 4 times greater than the corresponding  $\text{A}\leftarrow\text{X}$  (2,3) transition probability. Were  $\text{NO}(^2\Pi_\Omega)$  fragments produced equally populating the rotationally excited  $v = 1$  levels and relatively rotationally cold  $v = 3$  levels the underlying rotational progression of the (2,3) band would be observed in the REMPI spectrum (Fig. 3 (a)) with a peak intensity around a quarter of that of the (0,1) progression. The absence of such a progression and the signal-noise ratio in the recorded spectrum suggests that in fact the population of relatively rotationally cold levels of the (2,3) band must be less than  $2/3$  of that of the rotationally excited levels of the (0,1) band. Considering the intensity profile of the  $\text{O}(^3\text{P}_J)$  energy distributions and that the rotational profile of the (0,1) band is spread over more than 60 rotational levels, it seems likely that the population of the  $\text{NO}(^2\Pi_\Omega)$  in  $v = 3$  is actually significantly less than  $2/3$  that of the population of  $v = 1$ .

There are a number of potential complications to the analysis of the whole (0,1) rotational profile. Close to 5.55 eV, the photolysis energy is sufficient to produce  $\text{NO}(^2\Pi_{1/2})$  in  $v = 1$  in coincidence with  $\text{O}(^1\text{D}_2)$ . The rovibrational profiles of the  $\text{NO}(^2\Pi_\Omega)$  fragments produced concomitantly with  $\text{O}(^1\text{D}_2)$  have been probed between 5.41 and 5.71 eV.<sup>47,48</sup> These profiles are characterized by relatively statistical profiles with rotational temperatures between 200 and 400 K.<sup>47,48,51</sup> The dissociation via the  $\text{O}(^1\text{D}_2)$  channel favors the production of vibrationally inverted  $\text{NO}(^2\Pi_\Omega)$  fragments with relatively little energy partitioned into rotation (we will discuss this more fully in a subsequent publication)<sup>51</sup>. With the low rotational excitation of these  $\text{NO}(^2\Pi_\Omega)$  fragments in mind, there should be almost no population of rotational levels above  $N = 35$  in the  $\text{O}(^1\text{D}_2)$   $v = 1$  channel. These rotational levels would appear in the REMPI spectrum close to 5.28 eV, but this is below the energetic threshold for the production of  $\text{NO}(^2\Pi_\Omega)$  in  $v = 1$  with  $\text{O}(^1\text{D}_2)$  so they would not be observable in a single laser experiment. Furthermore,  $\text{NO}(^2\Pi_\Omega)$  produced in coincidence with  $\text{O}(^1\text{D}_2)$

should not have an effect on the rest of the (0,1)  $\text{NO}(^2\Pi_\Omega)$  with  $\text{O}(^3\text{P}_J)$  rotational profile, as  $\text{NO}(^2\Pi_\Omega)$  cannot be formed in  $v = 2$  with  $\text{O}(^1\text{D}_2)$  at excitation energies below 5.54466 eV. The result of this is that the entire (0,1) rotational profile in the REMPI spectrum is due to  $\text{NO}(^2\Pi_\Omega)$  fragments formed with  $\text{O}(^3\text{P}_J)$  fragments only. Despite this, further complications to the band structure could arise from its spectral width; the band spans a range between 5.23 to 5.44 eV. In this region signatures from  $\text{NO}(^2\Pi_\Omega)$  fragments formed with  $\text{O}(^3\text{P}_J)$  in  $v = 2, 3$  and 4 could also be observed. As we have discussed the contribution to the total  $\text{O}(^3\text{P}_J)$  signal from  $\text{NO}(^2\Pi_\Omega)$  fragments in  $v = 3$  must be small. On similar arguments the effect of  $\text{NO}(^2\Pi_\Omega)$  fragments in  $v = 2$  and 4 probed via the (1,2) and (3,4) bands can be assessed.

Analysis of the spectral region which corresponds to the rotationally cold part of the (1,2) band in the spectrum recorded by Im and Bernstein indicates that the population of these levels is less than 3/5 of the population of  $\text{NO}(^2\Pi_\Omega)$  fragments in  $v = 1$  and  $N \sim 42$ . If the (1,2) band were assumed to have a similar rotational profile to the (0,1) band, we would expect a primary peak in the distribution at an excitation energy of 5.42134 eV (228.697 nm). When spectra are recorded between 5.41 and 5.46 eV only very weak signals are observed. As very few of these rotational lines are above the level of the noise, the signatures of rotational profiles in this energy range are below the detection limit of our experiment. If the rotational profile of the  $\text{NO}(^2\Pi_\Omega)$  fragments in  $v = 2$  was similar to that of  $v = 1$ , it is likely that we would not be able to detect these photofragments via the (1,2) band as the transition probability for this band is almost 300 times smaller than that of the (0,1) band. The absence of any appreciable signal close to 5.42924 eV (228.364 nm) indicates that the population of fragments produced in  $v = 4$  with little rotational excitation must be less than  $\frac{3}{4}$  of the population of the rotationally excited  $\text{NO}(^2\Pi_\Omega)$  fragments in  $v = 1$ . Were the  $v = 4$  fragments to display a similar rotational profile to those in  $v = 1$ , a signature would be expected to be seen close to 5.54764 eV (223.490 nm). This would overlap with the (1,1) vibrational band, throughout which  $\text{NO}(^2\Pi_\Omega)$  can be produced in coincidence with  $\text{O}(^1\text{D}_2)$ . As the total  $\text{O}(^1\text{D}_2)$  channel makes up  $\sim 50\%$  of the total  $\text{NO}(^2\Pi_\Omega)$  signal in  $v = 0, 1$  or 2 at photolysis wavelengths which could probe the NO fragments in this band, it is unlikely that the underlying signature of rotationally excited fragments in  $v = 4$  could be observed in a single laser experiment due to the low signal intensity. For similar reasons, the underlying signatures of rotationally

excited  $\text{NO}(^2\Pi_\Omega)$  fragments in  $v = 0$  or  $3$  are unlikely to be observed in a one laser experiment due to the large signal from rotationally cold  $v = 2$  or  $0$  products formed with  $\text{O}(^1\text{D}_2)$  probed via the  $(2,2)$  and  $(0,0)$  bands.

We have argued that rotationally excited  $\text{NO}(^2\Pi_\Omega)$  fragments produced in  $v = 1$  have a greater contribution to the total  $\text{O}(^3\text{P}_j)$  signal than rotationally cold  $\text{NO}(^2\Pi_\Omega)$  fragments in  $v = 3$ . This should be evident in the energy distributions of the  $\text{O}(^3\text{P}_j)$  fragments. The expected kinetic energies of the  $\text{O}(^3\text{P}_j)$  fragments formed in coincidence  $\text{NO}(^2\Pi_\Omega)$  fragments in  $v = 1$  and  $N = 50$  and  $N = 65$  are drawn as dotted lines on the energy distributions in Figs. 2 (d) to (f). We see that this range of rotationally excited NO co-fragments span major peaks of the energy distributions of all three  $\text{O}(^3\text{P}_j)$  spin-orbit components. It should be noted that the spectrum in Fig. 3 (a) and those recorded by Im and Bernstein are primarily a reflection of the rotational profiles of the  $\text{O}(^3\text{P}_2)$  channel due to the spin-orbit product ratio. It is therefore expected that there should be good agreement between the rotational distribution recorded in Fig. 3 (a) with one of the main peaks in the  $\text{O}(^3\text{P}_2)$  energy distribution. The kinetic energy expected for peak of the rotational profile ( $N = 57$ ) is drawn on Fig. 2 (d)-(f) as a single dashed line. The major peak in the  $\text{O}(^3\text{P}_2)$  kinetic energy distribution (Fig. 2 (d)) matches exactly with the energy expected for the production of an O atom in coincidence with a  $^2\Pi_{1/2}$  NO co-fragment in  $v = 1$   $N = 57$ , i.e. the strongest line in the REMPI spectrum. Similarly for the shoulder of the main peak in the  $\text{O}(^3\text{P}_0)$  profile (Fig. 2 (f)). It was previously believed that on excitation at  $\sim 226$  nm to the  $(2)^2\text{B}_2$  state the  $\text{O}(^3\text{P}_j) + \text{NO}(^2\Pi_\Omega)$  dissociation channel led to a sharply peaked vibrational distribution with  $\text{NO}(^2\Pi_\Omega)$  fragments formed in  $v = 4-6$ . In fact, the  $\text{O}(^3\text{P}_2)$  distribution (the major  $\text{O}(^3\text{P}_j)$  spin-orbit product) peaks in coincidence with highly rotationally excited  $\text{NO}(^2\Pi_\Omega)$  fragments in  $v = 1$  and  $N \sim 57$ .

The other peaks in the O atom energy distributions are indicative of further structure in the rovibrational profiles of the  $\text{NO}(^2\Pi_\Omega)$  co-fragments. Provided there is no interference in the recorded  $\text{O}(^3\text{P}_2)$  distribution from species other than  $\text{NO}_2$  and that the absorption of a single photon led to dissociation, the peak at  $\sim 1.47$  eV (Fig. 2 (d); peak a) must be due to  $\text{O}(^3\text{P}_2)$  fragments formed in  $v = 0$  with a rotational quantum number close to  $N = 24$ . It seems likely that the peak at  $1.32$  eV (Fig. 2 (d); peak b) is then due to the production of  $\text{NO}(^2\Pi_{1/2})$  in  $v = 1$  due to the similarity in the rotational profile of this peak ( $N_{\text{max}} = 24$ ). A bimodal rotational profile (peaking at

$N \sim 57$  and  $N \sim 24$ ) is in agreement with the spectra recorded by Im and Bernstein between 229 and 236 nm.

With evidence for bimodality in the rotational profiles of the  $\text{NO}(^2\Pi_{\Omega})$  fragments formed in low  $v$  and the observation that the major dissociation pathway in the  $\text{O}(^3\text{P}_2)$  product channel produces highly rotationally excited  $\text{NO}(^2\Pi_{\Omega})$  fragments in  $v = 1$ , it would be reasonable to expect highly rotationally excited  $\text{NO}(^2\Pi_{\Omega})$  products in  $v = 0$  and also  $v = 2$ . Were the  $v = 2$  fragments to display the same bimodal rotational profile as the  $v = 1$  fragments with peaks at  $N \sim 24$  and  $57$ , peaks would be expected at 1.17 and 0.81 eV in the  $\text{O}(^3\text{P}_2)$  distribution. In fact prominent peaks are observed in the distribution at 1.19 and 0.81 eV (Fig. 2 (d), peaks c and f), corresponding to diatomic fragments in  $v = 2, N \sim 20$  and  $v = 2, N \sim 57$  respectively. With a similar argument, rotationally excited fragments ( $N = 57$ ) produced in  $v = 0$  would be expected to occur close to 1.10 eV. A major peak is observed in Fig. 2 (d) at 1.05 eV which would correlate with  $N \sim 60$ . With this in mind, the broad peak at 0.71 eV (Fig. 2 (d) peak g) likely correlates with  $\text{NO}(^2\Pi_{\Omega})$  fragments in  $v = 3$  with a maximum in the rotational profile occurring at  $N \sim 54$ . It would seem that a dissociation mechanism which promotes rotational excitation in fragments occupying the lower vibrational levels adequately explains the major features of the  $\text{O}(^3\text{P}_2)$  energy distribution. As might be expected in a mechanism favoring rotational excitation, fragments formed with vibrational excitation are generally formed with slightly less rotational excitation.<sup>52</sup>

Based on the bimodal rotational profile of the  $\text{NO}(^2\Pi_{\Omega})$  fragments in  $v = 1$ , there are likely other minor peaks due to rotationally cold fragments in Fig. 2 (d) which are somewhat masked by the more intense peaks in the  $\text{O}(^3\text{P}_2)$  energy distribution. Assuming similar rotational profiles for the different vibrational states, we expect a peak at 1.05 eV for fragments in  $v = 3$  and  $N \sim 20$ . This peak would form part of peak d. The contribution of such a peak to the distribution, however, must be very small (as is evident in Fig. 3 (a)) and a firm assignment would require the detection of the relevant  $\text{NO}(^2\Pi_{\Omega})$  co-fragments. There are no obvious features in the distribution which could be assigned to relatively rotationally cold fragments in  $v = 4, 5$  or  $6$ . It seems that the two rotational modes observed in the  $\text{O}(^3\text{P}_2)$  distribution share a similar vibrational profile.

The peak energies of the  $O(^3P_2)$  distribution and the co-fragment assignments are summarized in Table 2. A similar treatment has been carried out for the  $O(^3P_0)$  energy distribution (Fig. 2 (f)). This is summarized in Table 3. The main conclusion of the analysis of the energy distributions is that there appear to be two different dissociation mechanisms by which  $O(^3P_J)$  atoms can be formed with kinetic energies between 1.55 and 0.5 eV. The major mechanism forms vibrationally cold but rotationally hot  $NO(^2\Pi_{1/2})$  fragments with a minor mechanism forming rotationally colder diatomic products with a similar vibrational profile. The production of such highly rotationally excited products from the dissociation of the  $(2)^2B_2$  state has recently been predicted by Schinke and co-workers.<sup>4</sup>

### **3. Translational anisotropy of the $O(^3P_{2,0})$ fragments**

To support the interpretation of the  $O(^3P_{2,0})$  energy distributions, the anisotropies of the unaligned image features were analyzed using the well known formula introduced by Zare.<sup>53</sup> The structure in the unaligned  $O(^3P_{2,0})$  energy distributions allows the anisotropy of the image features to be individually assessed. The spatial anisotropy of each ring obtained by fitting radially averaged profiles as a function of the kinetic energy of the fragments is plotted in Fig. 6. The anisotropies of the  $O(^3P_2)$  and  $O(^3P_0)$  images display the same trends with kinetic energy release. Fragments with high kinetic energies have the highest anisotropy parameters (1.5 and 1.2 respectively) with the anisotropy decreasing to a minimum at 0.5 eV (0.5 and 0.6). However, below kinetic energies of 0.5 eV, the  $O(^3P_J)$  anisotropy parameter rises. This change in the trend of the anisotropy parameter below 0.5 eV is a clear indication of a difference, on average, in the dissociation mechanism as  $NO(^2\Pi_\Omega)$  fragments are formed with greater internal excitation.

Focusing on the anisotropies between 1.55 and 0.5 eV, we expect changes in the anisotropy parameter due to the different dissociation mechanisms which produce relatively rotationally cold and highly rotationally excited NO fragments. Peaks a, b and c in Figs. 2 (d) and (f) are assigned to  $O(^3P_{2,0})$  atoms produced in coincidence with  $NO(^2\Pi_\Omega)$  products in  $v = 0, 1$  and  $2$  with relatively little rotational excitation. Peaks d and e are primarily attributed to rotationally excited fragments produced via the major dissociation pathway; although there is likely underlying structure due to the minor dissociation pathway. Using a simple impulsive model of the dissociation

and assuming a 36 fs dissociation timescale (as supported by the work of Tsuji *et al.*<sup>26</sup> and Schinke *et al.*<sup>4</sup>), it would be expected that peaks d and e are the result of a more bent geometry at the point of dissociation. Conversely, peaks a, b and c should be the result of dissociation via a more linear parent geometry. We therefore expect that the anisotropy of rings a, b and c would be more anisotropic than rings d and e. This is indeed observed in Fig. 6 for peaks a, b, d and e. The large reduction of the anisotropy of ring c is rationalized by the large contribution of the underlying high kinetic energy tail of peak d due to diatomic fragments in  $v = 0$  and  $N \sim 50$ . At lower kinetic energies (0.50-0.90 eV) the anisotropy parameter reflects an average of the anisotropy due to rotationally cold  $\text{NO}(^2\Pi_{\Omega})$  products (potentially in  $v = 4, 5$  and  $6$ ), the anisotropy due to rotationally excited fragments in  $v = 2$  and importantly the highly rotationally excited tails of the rotational profiles which form peaks d and e. The resulting anisotropy is heavily weighted by highly rotationally excited fragments produced from  $\text{NO}_2$  dissociating with a reduced bond angle. As a result the anisotropy of the image features reduces as the kinetic energy of the fragments decreases to 0.50 eV.

The image features seen at kinetic energies below 0.50 eV appear to result from the dissociation of  $\text{NO}_2$  producing relatively rotationally cold  $\text{NO}(^2\Pi_{\Omega})$  fragments in  $v = 8-11$ . The appearance of these minor peaks is consistent with the observations of Ahmed *et al.* who also observed a second, competitive, dissociation channel in the  $\text{O}(^3\text{P}_j)$  distributions which produced internally excited NO fragments at a photolysis wavelength of 212.8 nm.<sup>39</sup> Similar peaks have been observed in the  $\text{O}(^3\text{P}_j)$  distributions close to 200 nm, where they dominate the distribution.<sup>41</sup> It would seem that this dissociation mechanism becomes more important as the photolysis wavelength is reduced from 226 to 200 nm. Close to 226 nm, the intensity of the  $\text{O}(^3\text{P}_j)$  signal at kinetic energies between 0 and 0.5 eV depends on the temperature of the source (see Fig. 5). So one must question whether or not peaks h, i and j in Figs. 2 (d) and (f) are due to interference from  $\text{N}_2\text{O}_4$ ; we do not believe so for the following reasons.

#### **4. The influence of the $\text{NO}_2/\text{N}_2\text{O}_4$ equilibrium**

The effects of the  $\text{NO}_2/\text{N}_2\text{O}_4$  equilibrium on the UV study of the photodissociation dynamics of  $\text{NO}_2$  have previously been discussed in the literature.<sup>16,54</sup> In our experiments, temperature studies (Fig. 5) reveal a broad unstructured underlying

feature in the  $O(^3P_2)$  kinetic energy profile at lower sample gas temperatures between 0 and 0.5 eV. This feature was prominent in the  $O(^3P_2)$  distribution with a significantly smaller contribution to the  $O(^3P_1)$  distribution and no contribution to the  $O(^3P_0)$  with a sample backing pressure of 1 bar, a  $NO_2$  partial pressure of 2% and a sample temperature of 295 K. The maximum of the feature occurs close to 0.1 eV. This broad feature is lost as the sample temperature is raised to  $\sim 400$  K (see Fig. 2 (d) to (f)). The feature has an overall anisotropy of  $0.2 \pm 0.1$ , which is in qualitative agreement with the results of Brouard *et al.* who observed a similar structure in the  $O(^3P_2)$  velocity profile with an anisotropy of 0.1 using a room temperature sample gas, a sample pressure of 2 bar and  $NO_2$  partial pressures of 10%, 1% and “trace quantities” in He.<sup>16</sup> Brouard and co-workers observed a decrease in the contribution of the broad unstructured component as the partial pressure of the  $NO_2$  in their sample was reduced. They used the spin-orbit ratio of Rubahn *et al.*<sup>29</sup> to normalize their speed distributions and hence to deduce that the 226 nm dissociation of  $N_2O_4$  produces almost exclusively  $O(^3P_2)$  atoms. In experiments in which we increase the total sample pressure behind our molecular beam source to 2 bar we also see a significant increase in the contribution of the broad unstructured component in the  $O(^3P_2)$  kinetic energy profile, in complete agreement with the observations of Brouard *et al.* With the higher resolution afforded by the DC slice imaging technique, however, we additionally observe three peaks on top of the broad background feature at 0.22, 0.25 and 0.37 eV (peaks h, i and j in Figs. 2 (d) and 2 (f)). The area under each of these peaks, unlike the underlying profile, is independent of temperature. This implies that these peaks are due to  $NO_2$  photolysis and not due to the photolysis of a contaminant. In separate experiments, the kinetic energy profile of the  $O(^3P_0)$  fragment distribution was recorded at 295 and 393 K. In this case the profile was found to be independent of temperature, supporting the interpretation that peaks h, i and j are due to  $NO_2$  photolysis.

In the presence of oxygen and helium and based on the thermodynamic stabilities of the oxides of nitrogen, the only important species in these experiments are NO and  $N_2O_4$ .<sup>55</sup> Furthermore, in a single laser experiment close to 226 nm the photolysis of NO to produce  $O(^3P_1)$  atoms can be considered unimportant.<sup>56</sup> At the laser fluence employed we can also discount any contribution from the dissociation of  $O_2$ .<sup>57</sup> As pointed out by Brouard *et al.*<sup>16</sup>, the reduction of the  $NO_2$  partial pressure in

the reagent mixture would push the  $\text{NO}_2/\text{N}_2\text{O}_4$  equilibrium to favour the monomer. Under the conditions employed by Brouard *et al.* (room temperature sample, 2 bar backing pressure),  $\text{NO}_2$  partial pressures of 10% and 1% result in 48% and 11% of the  $\text{NO}_2$  existing in its dimeric form. Given that the  $\text{N}_2\text{O}_4$  absorption cross-section is ten times that of  $\text{NO}_2$  close to 226 nm, we would expect the  $\text{N}_2\text{O}_4$  photolysis products to have a yield between 1 and 5 times those of  $\text{NO}_2$ . A partial pressure of 0.01% would be required to push the equilibrium 99.9% in favor of the monomer to bring the single photon  $\text{N}_2\text{O}_4$  photolysis yield to the sub 1% level. It is therefore unsurprising that in the experiments of Brouard and co-workers, using “trace amounts” of  $\text{NO}_2$  did not remove the broad unstructured slow component in the  $\text{O}(^3\text{P}_2)$  kinetic energy profile.

An alternative way of pushing the equilibrium of the sample gas towards the monomer is to increase its temperature. With a backing pressure of 1 bar and a  $\text{NO}_2$  partial pressure of 2% sample temperatures of 298 and 345 K result in ~20% and ~2% of the  $\text{NO}_2$  existing in dimeric form. We might therefore expect the single photon photolysis yield of  $\text{N}_2\text{O}_4$  products to increase by a factor of 10 as the temperature is decreased from 345 to 298 K. In fact we observe an increase of about 3.3 which would be consistent, within the experimental uncertainty, with the dissociation of  $\text{N}_2\text{O}_4$  via a two photon excitation (with an expected increase of  $\sqrt{10}$ ). The anisotropy between 0 and 0.5 eV represents the average of the anisotropy of the temperature dependent feature and peaks h, i and j. The anisotropies of peaks h, i and j are shown in Fig. 6;  $\beta \sim 0.5\text{-}0.8$ . As we measure an average anisotropy value of 0.2 between 0 and 0.5 eV at 298 K, we can consider the temperature dependent feature to be essentially isotropic. The kinetic energy profile and anisotropies of the slow  $\text{O}(^3\text{P}_2)$  atoms suggests that they are either produced by a threshold dissociation process following two photon absorption of  $\text{N}_2\text{O}_4$  in which the co-fragment is formed with large internal excitation or that the  $\text{O}(^3\text{P}_2)$  atoms are formed from an  $\text{NO}_2$  photoproduct produced by the one photon dissociation of  $\text{N}_2\text{O}_4$  in a secondary step. We cannot definitively identify the dissociation mechanism. We therefore assign the broad peak to  $\text{N}_2\text{O}_4$  photolysis by either of the above mechanisms and peaks h, i and j to a dissociation process of the monomer. Without detection of the NO co-fragments for the peaks h, i and j in Figs. 2 (d) and (f) and Fig. 5 the rovibrational profiles of these peaks cannot be definitively assigned.

## 5. Dissociation mechanisms

The calculations of Schinke *et al.* reveal the mechanism for the production of vibrationally cold, highly rotationally excited  $\text{NO}(^2\Pi_{\Omega})$  products (the major dissociation products close to 226 nm).<sup>4</sup> The Franck-Condon window to the parent  $(2)^2B_2$  state occurs at the repulsive wall of the potential and sets up motion in the bound symmetric stretching coordinate. At the other side of the potential the motion of the  $\text{NO}_2$  is deflected towards the dissociative asymmetric stretching coordinate with the dissociation taking place on the timescale of a single symmetric stretch vibration ( $\sim 35$  fs). The vibrational excitation produced due to the position of the Franck-Condon window and the excess energy in the  $(2)^2B_2$  potential is retained in the dissociation, primarily producing  $\text{NO}(^2\Pi_{\Omega})$  in  $v = 0$  or 1. The narrow, inverted rotational profiles are then explained by the impulsive model with the torque for NO rotation increasing as the  $\text{NO}_2$  bond angle decreases along the bending coordinate. The anisotropy of the relevant  $\text{O}(^3P_2)$  image features imply that the average bond angle of the  $\text{NO}_2$  as it dissociates on the adiabatic  $(2)^2B_2$  surface via the major pathway lies between  $118$  and  $129^\circ$ .

At higher excitation energies the vibrational energy of this major dissociation channel increases as the initial excitation occurs higher in the  $(2)^2B_2$  state resulting in a greater degree of symmetric stretch excitation. The rotational energy is calculated to remain relatively constant.<sup>4</sup> The overall change in internal energy should be approximately described by the solid line in Fig. 1. The major peak in the  $\text{O}(^3P_1)$  distribution recorded by Ahmed *et al.* close to  $213\text{ nm}^{39}$  (at a  $\text{O}(^3P_1)$  kinetic energy of  $1.18\text{ eV}$ ) can therefore be attributed to  $\text{NO}(^2\Pi_{\Omega})$  fragments produced in  $v = 2$  and  $N \sim 53$ . The secondary peak in the  $\text{O}(^3P_1)$  distributions recorded by Coriou *et al.*<sup>41</sup> (at total fragment kinetic energies close to  $1.24\text{ eV}$ ) can similarly be assigned to production in coincidence with  $\text{NO}(^2\Pi_{\Omega})$  in  $v = 5$  and  $N \sim 59$ . This correlates with the experiments of Hancock and Morrison at slightly higher excitation energy where the major peak in the vibrational profile occurs at  $v = 5$  (although the vibrational profile is convoluted with the profile of the  $\text{O}(^1D_2)$  co-fragments).<sup>25</sup> At this excitation wavelength we would expect a rotational distribution peaking at a rotational level close to  $N = 60$ , as predicted by Schinke *et al.*<sup>4</sup>

An explanation for the production of the rotationally cold  $\text{NO}(^2\Pi_{\Omega})$  fragments in low vibrational levels (peaks a, b and c in Fig. 2 (d) and (f)) and those produced highly internally excited (peaks h, i and j in Fig. 2 (d) and (f)) is not forthcoming from the results of Schinke *et al.*<sup>4</sup> When the intensities of peaks a, b and c are analyzed in the three  $\text{O}(^3\text{P}_J)$  images we measure a spin-orbit ratio of 1.00:0.65:0.15, which is in good agreement with the overall spin-orbit ratio measured for the fragments with kinetic energies between 0.50 and 1.10 eV (peaks d-g). The vibrational profile of the fragments produced by this secondary dissociation mechanism is similar to that of the major pathway (mainly  $v = 0-2$ ). Presumably the vibrational profile of the secondary dissociation mechanism is also determined early in the dissociation by the position of the Franck-Condon window on the  $(2)^2\text{B}_2$  potential. It therefore appears that there are two different pathways coupling the diabatic  $(2)^2\text{B}_2$  state to  $\text{NO}(^2\Pi_{\Omega}) + \text{O}(^3\text{P}_J)$ . Two different rotational profiles result with the minor profile being due to dissociation via a more linear geometry. The similarity of the spin-orbit ratios for the two dissociation mechanisms implies that the spin-orbit branching is determined late in the dissociation.

The temperature studies strongly suggest that the  $\text{O}(^3\text{P}_J)$  peaks produced with highly internally excited  $\text{NO}(^2\Pi_{\Omega})$  fragments are due to  $\text{NO}_2$  photolysis at 226 nm. A more accurate investigation of the origin of these peaks could be carried out at higher excitation energies where they are prominent in the photofragment distributions and thermodynamic effects should be more obvious. It is expected that the  $\text{O}(^3\text{P}_J)$  distributions measured with a room temperature sample, a total gas pressure of  $\sim 1$  bar and  $\text{NO}_2$  partial pressures close to 2% between 213 and 193 nm would contain between five and ten times more signal from two photon  $\text{N}_2\text{O}_4$  photolysis than at 226 nm. These effects are evident in the results of Ahmed *et al.*<sup>39</sup> and Coriou *et al.*<sup>41</sup>, who observe broad underlying features in the  $\text{O}(^3\text{P}_J)$  kinetic energy distributions close to 213 and 201 nm respectively. The wavelength dependence of the intensity ratio of the broad underlying component and the sharp features at low kinetic energies in the  $\text{O}(^3\text{P}_J)$  profiles provides further evidence that these features have different origins.

A final consideration is the difference between the spin-orbit ratios measured in this study and those recorded by Rubahn *et al.* close to 226 nm<sup>29</sup> and Miyawaki *et al.* close to 213 nm<sup>58</sup>. The overall spin-orbit ratio determined at 393 K in this study is 1.00:0.71:0.15 and is the result of the photolysis of a beam containing

~0.1% N<sub>2</sub>O<sub>4</sub>. The room temperature gas mixtures used in the molecular beam studies carried out by Rubahn *et al.* and Miyawaki *et al.* resulted in different concentrations of N<sub>2</sub>O<sub>4</sub> at their laser interaction regions. Based on the experimental conditions it is expected that the N<sub>2</sub>O<sub>4</sub> concentration should be significantly higher in the experiments of Miyawaki *et al.* (between 19.4% and 48.5% of the total NO<sub>2</sub>) in comparison to the studies of Rubahn *et al.* (between 8.8% and 32.4% of the total NO<sub>2</sub>). The effect of the N<sub>2</sub>O<sub>4</sub> is expected to be around five times greater in the studies of Miyawaki *et al.* due to the increase in the (single photon) N<sub>2</sub>O<sub>4</sub> absorption cross-section between 226 and 213 nm. The results of Brouard *et al.*<sup>16</sup> and those obtained in this study suggest that the 226 nm photolysis of N<sub>2</sub>O<sub>4</sub> produces O(<sup>3</sup>P<sub>J</sub>) photoproducts with a spin-orbit ratio heavily weighted in favor of the O(<sup>3</sup>P<sub>2</sub>) fragment. As all of the spin-orbit ratios are normalized with respect to the O(<sup>3</sup>P<sub>2</sub>) fragment the affects of N<sub>2</sub>O<sub>4</sub> photolysis should be observed as decreases in the relative O(<sup>3</sup>P<sub>1</sub>) and O(<sup>3</sup>P<sub>0</sub>) signals. This effect is most obvious in the strong O(<sup>3</sup>P<sub>1</sub>) signal which decreases, as expected, as the N<sub>2</sub>O<sub>4</sub> percentage and its absorption cross-section increase (0.71, 0.50 and 0.35 for 0.1% at 226 nm, 8-33% at 226 nm and 19-49% at 213 nm respectively). The effect is less obvious in the weak O(<sup>3</sup>P<sub>0</sub>) signal, the intensity of which will be particularly sensitive to the probe laser power and the experimental signal to noise ratio. These results further illustrate the advantages of kinetic energy resolved detection of photofragments as afforded by the VMI technique.

## V. Conclusions

The dissociation dynamics of NO<sub>2</sub> to produce NO(<sup>2</sup>Π<sub>Ω</sub>) and O(<sup>3</sup>P<sub>J</sub>) have been studied on excitation to the (2)<sup>2</sup>B<sub>2</sub> state close to 226 nm using REMPI spectroscopy, DC slice and conventional velocity map ion imaging. It was previously believed that on excitation at ~226 nm to the (2)<sup>2</sup>B<sub>2</sub> state the O(<sup>3</sup>P<sub>J</sub>) + NO(<sup>2</sup>Π<sub>Ω</sub>) dissociation channel led to a sharply peaked vibrational distribution with NO(<sup>2</sup>Π<sub>Ω</sub>) fragments formed in  $v = 4-6$ . In contrast to these previous studies, the high resolution achieved by DC slice imaging of O(<sup>3</sup>P<sub>J</sub>) fragments coupled with REMPI spectroscopy and velocity map imaging of state selected NO fragments reveals that the dissociation favors the production of highly rotationally excited NO(<sup>2</sup>Π<sub>Ω</sub>) fragments. All three O(<sup>3</sup>P<sub>J</sub>) spin-orbit component energy distributions are found to peak in coincidence with NO(<sup>2</sup>Π<sub>Ω</sub>) fragments in  $v = 0$  and 1 and  $N \sim 60$ , with a secondary rotational maxima at  $N \sim 20$ . The translational anisotropy of the fragments has been examined to conclude that the

dissociative geometry becomes more bent (on average) as the kinetic energy release of the  $O(^3P_J)$  decreases from 1.55 to 0.5 eV. The increase in the anisotropy parameter from 0.50 to 0 eV has been attributed to another minor dissociation mechanism producing kinetically cold  $O(^3P_J)$  in coincidence with internally excited NO fragments.

The spin-orbit branching ratio in the  $O(^3P_J)$  photoproducts is found to be markedly non-statistical. For O fragments with a translational energy in the range 0.50 to 1.55 eV the intensities of the three channels (uncorrected for degeneracy and line-strength factors) are determined to be 1.00:0.71:0.15 for the  $O(^3P_2)$ ,  $O(^3P_1)$  and  $O(^3P_0)$  states respectively. Another set of oxygen atoms with translational energies in the range 0.00 to 0.50 eV are also observed. The intensity ratio for these photoproducts is found to be 1.00:0.47:0.1. Temperature studies have highlighted that these fragments are correlated with internally excited  $NO(^2\Pi_Q)$  fragments produced from  $NO_2$ . The yield of these photofragments is noted to increase with excitation energy. Temperature studies have also demonstrated that the room temperature study of the UV  $NO_2$  photodissociation dynamics can be biased by the photolysis of  $N_2O_4$ .

## Acknowledgements

IW is grateful to the Engineering and Physical Sciences Research Council (EPSRC) for a research studentship. We are also indebted to Mr Panagiotis Kapatanopoulos for the design and construction of the high speed pulser unit used to gate the microchannel plates and to Dr Ivan Anton-Garcia for assistance in constructing the VMI spectrometer. This work has been supported by EPSRC grant EP/G000360/1.

## References

- 1 W. C. Gardiner Jr., *Gas-Phase Combustion Chemistry*. (Springer, 1999).
- 2 B. J. Finlayson-Pitts and J. N. Pitts, *Chemistry of the Upper and Lower Atmosphere: Theory, Experiments, and Applications*. (Academic Press, 1999).
- 3 J. Rolke, N. Cann, Y. Zheng, B. P. Hollebone, C. E. Brion, Y. A. Wang, and E. R. Davidson, *Chem. Phys.* **201**, 1 (1995).
- 4 R. Schinke, S. Y. Grebenshchikov, and H. Zhu, *Chem. Phys.* **346**, 99 (2008).
- 5 R. Jost, M. Joyeux, and M. Jacon, *Chem. Phys.* **283**, 17 (2002).
- 6 W. Schneider, G. K. Moortgat, G. S. Tyndall, and J. P. Burrows, *J. Photochem. Photobiol., A* **40**, 195 (1987).
- 7 A. C. Vandaele, C. Hermans, P. C. Simon, M. Carleer, R. Colin, S. Fally, M. F. Merienne, A. Jenouvrier, and B. Coquart, *J. Quant. Spectrosc. Radiat. Transfer* **59**, 171 (1998).
- 8 M. F. Merienne, A. Jenouvrier, B. Coquart, and J. P. Lux, *J. Atmos. Chem.* **27**, 219 (1997).
- 9 J. W. Au and C. E. Brion, *Chem. Phys.* **218**, 109 (1997).
- 10 G. E. Busch and K. R. Wilson, *J. Chem. Phys.* **56**, 3638 (1972).
- 11 R. Jost, J. Nygard, A. Pasinski, and A. Delon, *J. Chem. Phys.* **105**, 1287 (1996).
- 12 K. P. Huber and G. Herzberg, *Molecular Spectra and Molecular Structure IV. Constants of Diatomic Molecules*. (Van Nostrand Reinhold Company Inc., New York, 1979).
- 13 Y. Ralchenko, A. E. Kramida, J. Reader, and N. A. Team, (National Institute of Standards and Technology, 2008).
- 14 G. E. Busch and K. R. Wilson, *J. Chem. Phys.* **56**, 3626 (1972).
- 15 G. Herzberg, *Molecular Spectra and Molecular Structure Volume III - Electronic Spectra and Electronic Structure of Polyatomic Molecules*. (Krieger, Malabar, Florida, 1966).
- 16 M. Brouard, R. Cireasa, A. P. Clark, T. J. Preston, and C. Vallance, *J. Chem. Phys.* **124**, 064309/1 (2006).
- 17 G. Inoue, Y. Nakata, Y. Usui, H. Akimoto, and M. Okuda, *J. Chem. Phys.* **70**, 3689 (1979).
- 18 J. A. Mueller, M. L. Morton, S. L. Curry, J. P. D. Abbatt, and L. J. Butler, *J. Phys. Chem. A* **104**, 4825 (2000).
- 19 L. Harris and G. W. King, *J. Chem. Phys.* **8**, 775 (1940).
- 20 R. K. Ritchie, A. D. Walsh, and P. A. Warsop, *Proc. Roy. Soc. (London) Ser. A* **266**, 257 (1962).
- 21 R. S. Mulliken, *Rev. Mod. Phys.* **14**, 204 (1942).
- 22 T. Nakayama, M. Y. Kitamura, and K. Watanabe, *J. Chem. Phys.* **30**, 1180 (1959).

- 23 A. D. Walsh, J. Chem. soc., 2266 (1953).
- 24 W. M. Uselman and E. K. C. Lee, J. Chem. Phys. **65**, 1948 (1976).
- 25 G. Hancock and M. Morrison, Mol. Phys. **103**, 1727 (2005).
- 26 K. Tsuji, M. Ikeda, J. Awamura, A. Kawai, and K. Shibuya, Chem. Phys. Lett. **374**, 601 (2003).
- 27 K. F. Preston and R. J. Cvetanovic, J. Chem. Phys. **45**, 2888 (1966).
- 28 F. Sun, G. P. Glass, and R. F. Curl, Chem. Phys. Lett. **337**, 72 (2001).
- 29 H. G. Rubahn, W. J. Van Der Zande, R. Zhang, M. J. Bronikowski, and R. N. Zare, Chem. Phys. Lett. **186**, 154 (1991).
- 30 J. Miyawaki, K. Yamanouchi, and S. Tsuchiya, J. Chem. Phys. **99**, 254 (1993).
- 31 C. B. Mckendrick, C. Fotakis, and R. J. Donovan, J. Photochem. **20**, 175 (1982).
- 32 T. G. Slinger, W. K. Bischel, and M. J. Dyer, J. Chem. Phys. **79**, 2231 (1983).
- 33 J. Mcfarlane, J. C. Polanyi, and J. G. Shapter, J. Photochem. Photobiol. A Chem. **58**, 139 (1991).
- 34 M. Ahmed, D. S. Peterka, and A. G. Suits, in *Atomic and Molecular Beams*, edited by R. Campargue (Springer-Verlag, Berlin, 2001), pp. 343.
- 35 C. Morrell, C. Breheny, V. Haverd, A. Cawley, and G. Hancock, J. Chem. Phys. **117**, 11121 (2002).
- 36 B. F. Parsons, S. L. Curry, J. A. Mueller, P. C. Ray, and L. J. Butler, J. Chem. Phys. **111**, 8486 (1999).
- 37 M. Kawasaki, H. Sato, A. Fukuroda, T. Kikuchi, S. Kobayashi, and T. Arikawa, J. Chem. Phys. **86**, 4431 (1987).
- 38 W. N. Sisk, C. E. Miller, and H. S. Johnston, J. Phys. Chem. **97**, 9916 (1993).
- 39 M. Ahmed, D. S. Peterka, A. S. Bracker, O. S. Vasyutinskii, and A. G. Suits, J. Chem. Phys. **110**, 4115 (1999).
- 40 R. C. Richter, V. I. Khamaganov, and A. J. Hynes, Chem. Phys. Lett. **319**, 341 (2000).
- 41 A. M. Coroiu, D. H. Parker, G. C. Groenenboom, J. Barr, I. T. Novalbos, and B. J. Whitaker, Eur. Phys. J. D: At. Mol. Opt. Phys. **38**, 151 (2006).
- 42 D. Townsend, M. P. Minitti, and A. G. Suits, Rev. Sci. Instrum. **74**, 2530 (2003).
- 43 E. Wrede, S. Laubach, S. Schulenburg, A. Brown, E. R. Wouters, A. J. Orr-Ewing, and M. N. R. Ashfold, J. Chem. Phys. **114**, 2629 (2001).
- 44 N. Yonekura, C. Gebauer, H. Kohguchi, and T. Suzuki, Rev. Sci. Instrum. **70**, 3265 (1999).
- 45 A. T. J. B. Eppink and D. H. Parker, Rev. Sci. Instrum. **68**, 3477 (1997).
- 46 *Imaging in Molecular Dynamics: Technology and Applications*, edited by B. J. Whitaker (Cambridge University Press, 2003).
- 47 H. S. Im and E. R. Bernstein, J. Phys. Chem. A **106**, 7565 (2002).

- 48 L. Bigio, R. S. Tapper, and E. R. Grant, *J. Phys. Chem.* **88**, 1271 (1984).
- 49 C. Amiot, *J. Mol. Spectrosc.* **94**, 150 (1982).
- 50 J. Luque and D. R. Crosley, *LIFBASE: Database and Spectral Simulation Program* (SRI, 1999).
- 51 I. Wilkinson and B. J. Whitaker, (in preparation).
- 52 R. Schinke, *Photodissociation Dynamics*. (Cambridge University Press, 1993).
- 53 R. N. Zare, *Angular Momentum, understanding spatial aspects in chemistry and physics*. (John Wiley & Sons, Inc., New York, 1988).
- 54 A. T. J. B. Eppink, B. J. Whitaker, E. Gloaguen, B. Soep, A. M. Coroiu, and D. H. Parker, *J. Chem. Phys.* **121**, 7776 (2004).
- 55 N. N. Greenwood and A. Earnshaw, *Chemistry of the Elements*. (Butterworth-Heinemann, 1995).
- 56 B. L. G. Bakker, A. T. J. B. Eppink, D. H. Parker, M. L. Costen, G. Hancock, and G. A. D. Ritchie, *Chem. Phys. Lett.* **283**, 319 (1998).
- 57 B. Buijsse, W. J. Van Der Zande, A. T. J. B. Eppink, D. H. Parker, B. R. Lewis, and S. T. Gibson, *J. Chem. Phys.* **108**, 7229 (1998).
- 58 J. Miyawaki, T. Tsuchizawa, K. Yamanouchi, and S. Tsuchiya, *Chem. Phys. Lett.* **165**, 168 (1990).

## Tables

| <b>A←X</b><br><b>vibrational band</b> | <b>bandhead / eV</b> | <b>transition probability</b> |
|---------------------------------------|----------------------|-------------------------------|
| (3,3)                                 | 5.65147              | $6.186 \times 10^{-4}$        |
| (2,2)                                 | 5.59478              | $2.624 \times 10^{-3}$        |
| (1,1)                                 | 5.53765              | $1.610 \times 10^{-3}$        |
| (0,0)                                 | 5.47989              | $2.389 \times 10^{-3}$        |
| (3,4)                                 | 5.42924              | $1.807 \times 10^{-3}$        |
| (2,3)                                 | 5.36921              | $1.178 \times 10^{-3}$        |
| (1,2)                                 | 5.30850              | $1.671 \times 10^{-5}$        |
| (0,1)                                 | 5.24723              | $4.909 \times 10^{-3}$        |

Table 1 Transition probabilities and excitation energies for selected vibrational bands in the A←X absorption spectrum of NO. The data are taken from constants published in the LIFBASE spectral simulation program.<sup>50</sup>

| kinetic energy / eV | v | $\sim N_{\max}$ | peak |
|---------------------|---|-----------------|------|
| 1.47                | 0 | 24              | a    |
| 1.32                | 1 | 24              | b    |
| 1.19                | 2 | 20              | c    |
| 1.05                | 0 | 60              | d    |
| 0.95                | 1 | 57              | e    |
| 0.81                | 2 | 57              | f    |
| 0.71                | 3 | 54              | g    |
| 0.38                | ? | ?               | h    |
| 0.25                | ? | ?               | i    |
| 0.12                | ? | ?               | j    |

Table 2 Vibrational and rotational assignments of the NO co-fragment responsible for the peaks occurring in the  $O(^3P_2)$  kinetic energy release spectrum (Fig. 2 (d)).

| kinetic energy / eV | $\nu$ | $\sim N_{\max}$ | peak |
|---------------------|-------|-----------------|------|
| 1.44                | 0     | 26              | a    |
| 1.30                | 1     | 26              | b    |
| 1.19                | 2     | 20              | c    |
| 1.03                | 0     | 61              | d    |
| 0.92                | 1     | 58              | e    |
| 0.83                | 2     | 55              | f    |
| 0.73                | 3     | 52              | g    |
| 0.37                | ?     | ?               | h    |
| 0.25                | ?     | ?               | i    |
| 0.11                | ?     | ?               | j    |

Table 3 As Table 2 but for the  $O(^3P_0)$  kinetic energy release spectrum (Fig. 2 (f)).

## Figure Captions

FIG. 1:

Peak internal energy of the  $\text{NO}(^2\Pi_{\Omega})$  fragments produced in coincidence with  $\text{O}(^3\text{P}_j)$  for two different dissociation channels (high internal energy, low internal energy) at different excess energies in the  $(2)^2\text{B}_2$  state. The figure compares previous studies; McFarlane [<sup>33</sup>], Ahmed (1) [<sup>34</sup>], Brouard [<sup>16</sup>], Ahmed (2) [<sup>39</sup>], Coriou [<sup>41</sup>] and Hancock [<sup>25</sup>]; with this work. The error bars represent the half-width half-maximum of the internal energy distributions reported in these studies. In the experiments of Hancock and Morrison<sup>25</sup> only vibrational profiles were recorded. In this case the rotational energy corresponding to  $N \sim 57$  has been added to the most probable vibrational energy for the low internal energy channel (to give a total internal energy of  $\sim 1.82$  eV). This point is drawn as a filled triangle. The lines drawn through the points are quadratic least squares fits but are merely a guide to the eye and have no physical significance. The solid line links data for the channel producing fast O atoms. The dashed line links data for the channel producing slow O atoms.

FIG. 2:

DC slice velocity map images of the  $\text{O}(^3\text{P}_2)$ ,  $\text{O}(^3\text{P}_1)$  and  $\text{O}(^3\text{P}_0)$  fragments, respectively (a), (b) and (c), recorded using a single laser for both photolysis of the parent  $\text{NO}_2$  molecule and photo-ionization of the O fragment. The laser, which is polarized vertically to the image plane, is scanned over approximately 0.016 nm around each ionization resonance in order to ensure that the entire Doppler profile of the O fragments is evenly sampled. Each image is recorded for  $\sim 150\,000$  laser shots. Panel (d) shows the  $\text{O}(^3\text{P}_2)$  translational energy distribution produced from the photodissociation of  $\text{NO}_2$  via the  $(2)^2\text{B}_2$  state with associated peak labels as discussed in the text. The distribution is simply obtained by angular integration of the corresponding image (Fig. 2 (a)), multiplication by the appropriate Jacobian,  $r \sin(\vartheta)$ , and calibrated against a known kinetic energy release spectrum, usually of O atoms from the  $\sim 226$  nm photodissociation of  $\text{O}_2$ , recorded immediately prior or post the image acquisition with exactly the same extraction voltages and laser/molecular beam intersection point. Panels (e) and (f) show the photofragment distributions as in (d) but for the  $\text{O}(^3\text{P}_1)$  and  $\text{O}(^3\text{P}_0)$  fragments respectively.

FIG. 3:

Panel (a) mass-resolved (time-of-flight) REMPI excitation spectrum of  $\text{NO}(^2\Pi_\Omega)$  recorded at single photon excitation energies spanning the range of the (2,3)  $A\leftarrow X$  transition. Peak separations are noted to be around 4.6 meV. The expected position of the (2,3) band head is superimposed on the spectrum as a dashed vertical line at  $\sim 5.37193$  eV. The lines in the spectrum marked a, b, and c correspond to the excitation energies used to record the images presented in Fig. 4. Panels (b) and (c) show simulated NO absorption spectra for the NO  $A\leftarrow X$  transition using the LIFBASE spectral simulation software package.<sup>50</sup> Panel (b) shows the absorption of NO fragments produced in  $v = 3$  with a peak in a statistical rotational distribution at  $N = 21$ , while (c) shows the absorption of NO fragments produced in  $v = 1$  with a sharp rotational profile peaking at  $N \sim 57$  with a full-width half-maximum corresponding to the energy spread of 10 rotational levels.

FIG. 4:

Representative velocity map images and corresponding kinetic energy release spectra of NO fragments formed at excitation energies close to 230 nm (a, b and c in Fig. 3). The kinetic energy release of these fragments is too high for the fragments to be rotationally hot  $\text{NO}(^2\Pi_\Omega)$  radicals in  $v = 3$ . These NO fragments must be in the 2, 1 or 0 vibrational states. See text for discussion.

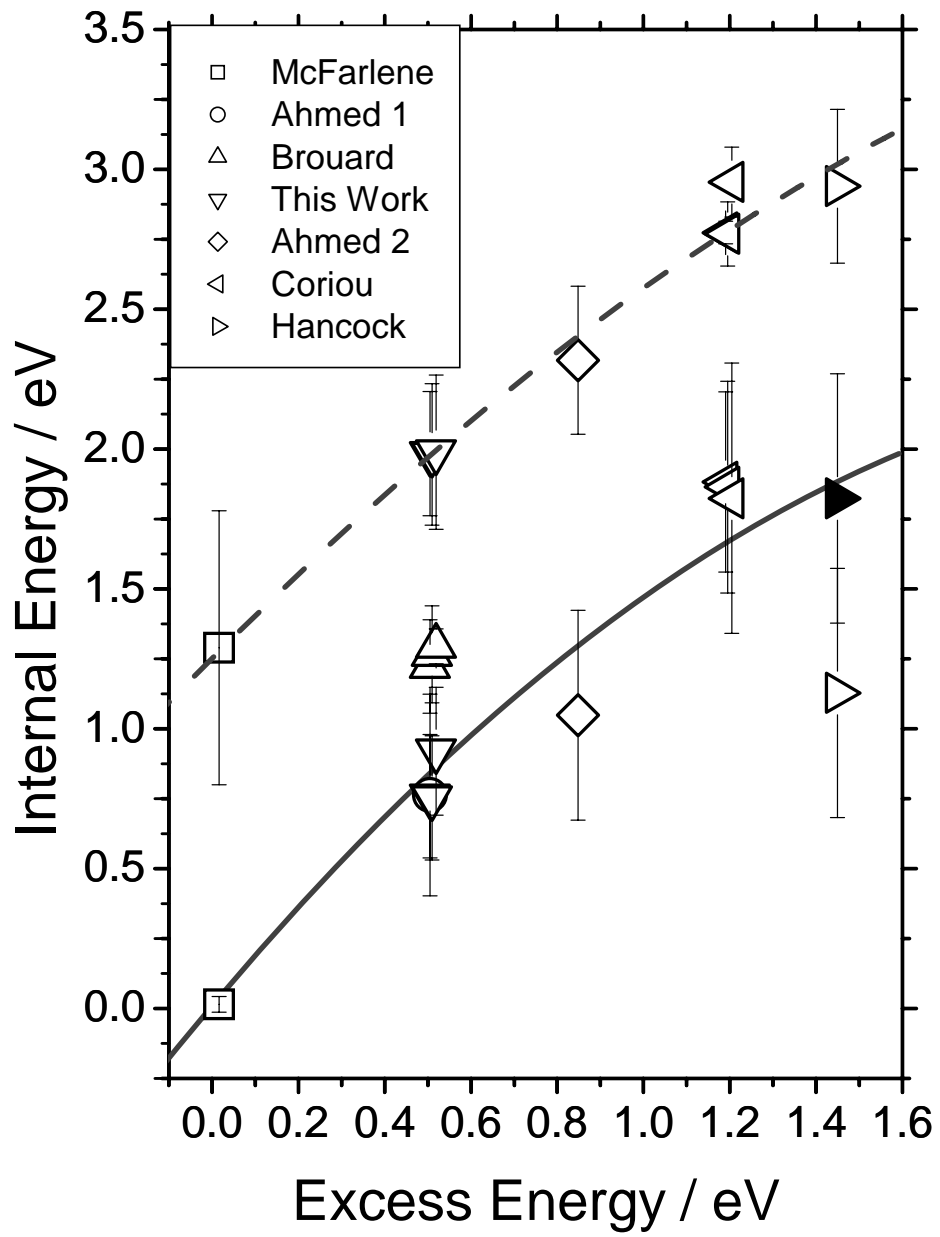
FIG. 5:

$\text{O}(^3P_2)$  energy release spectra recorded at a backing pressure of 1 bar and nozzle temperatures of 295 K (dotted line), 345 K (dashed line) and 393 K (solid line).

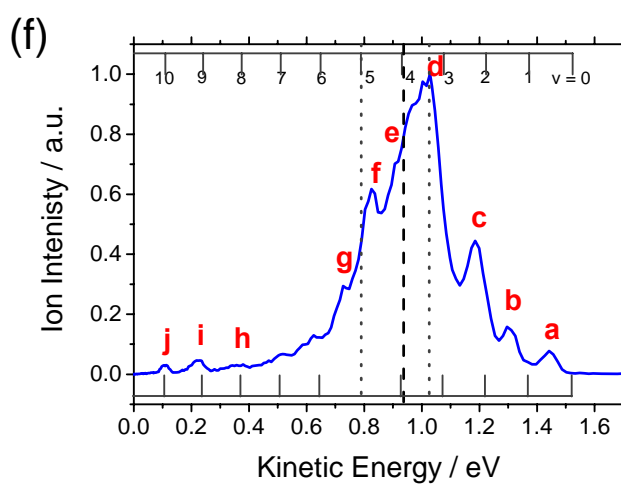
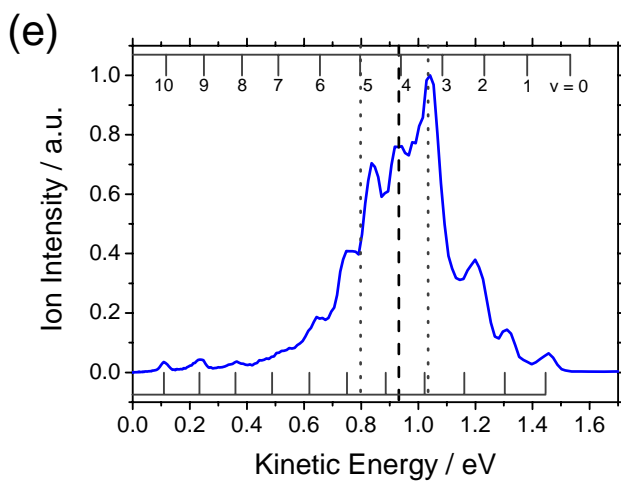
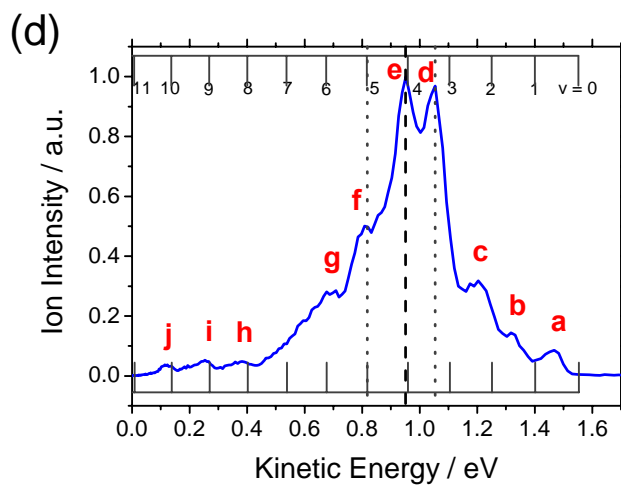
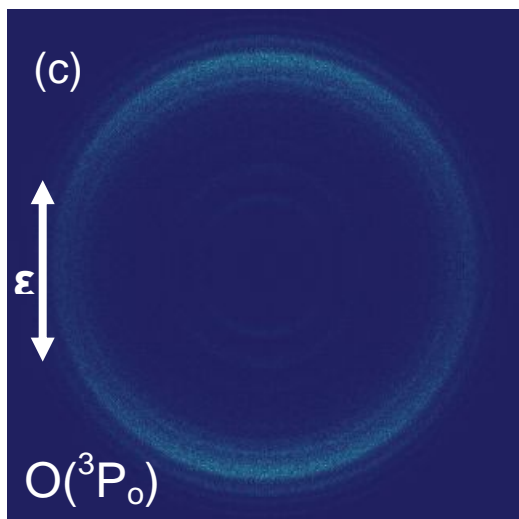
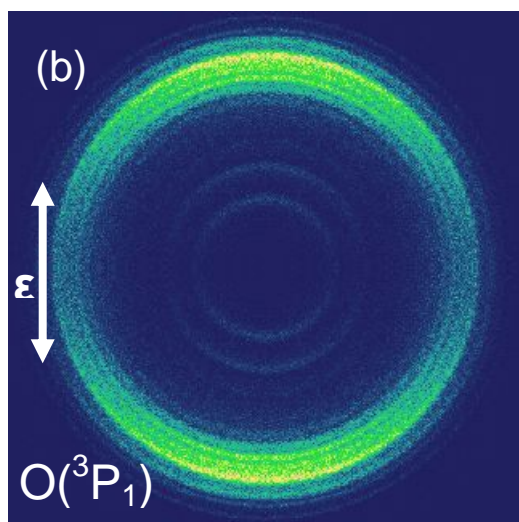
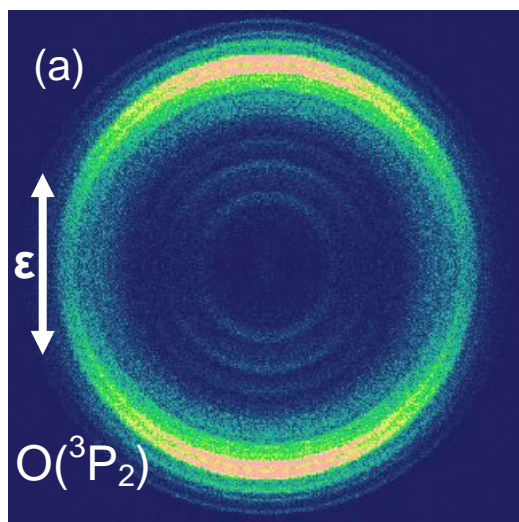
FIG. 6:

$\text{O}(^3P_2)$  and  $\text{O}(^3P_0)$  translational anisotropies as a function of the kinetic energy release.

# Figures

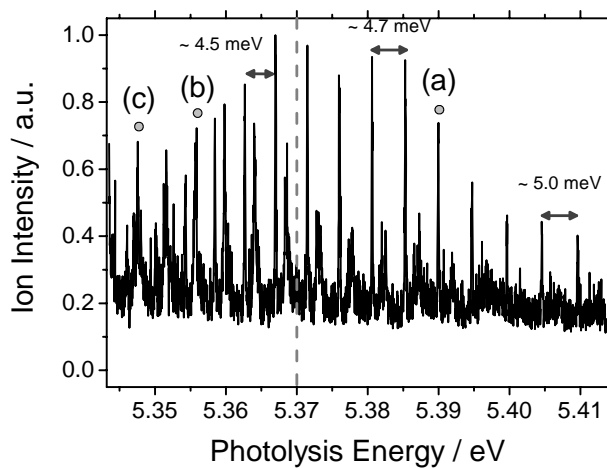


Wilkinson & Whitaker Figure 1

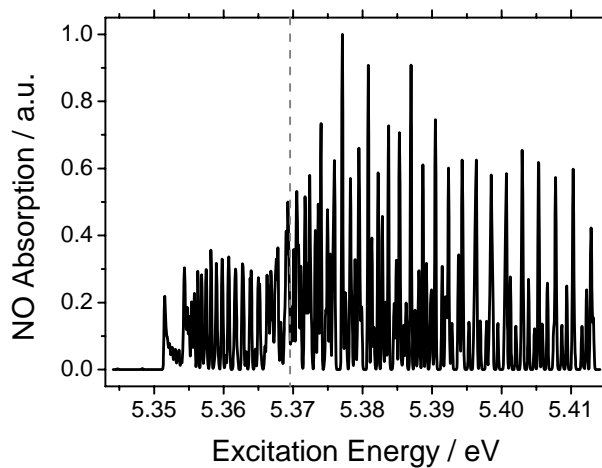


Wilkinson & Whitaker Figure 2

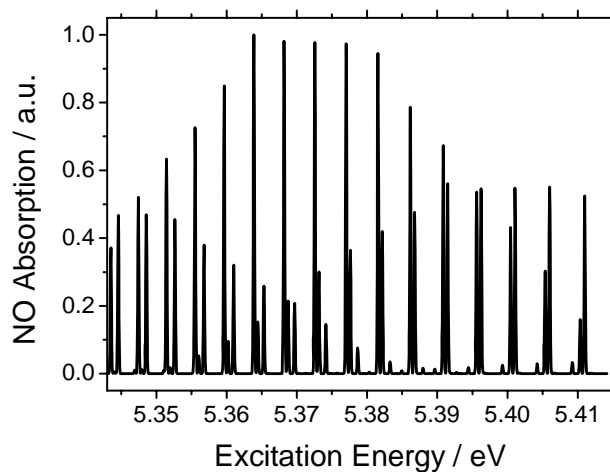
(a)



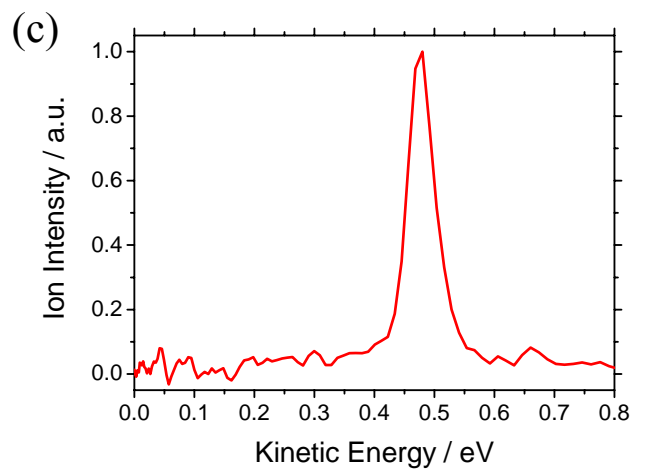
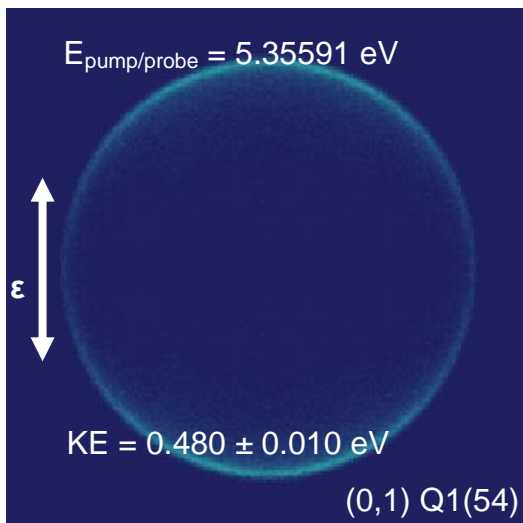
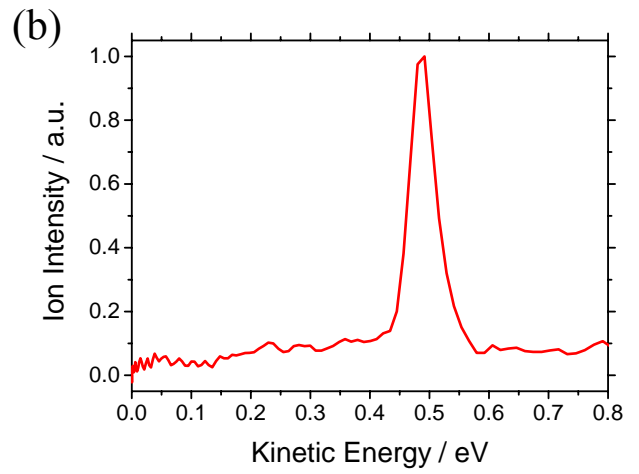
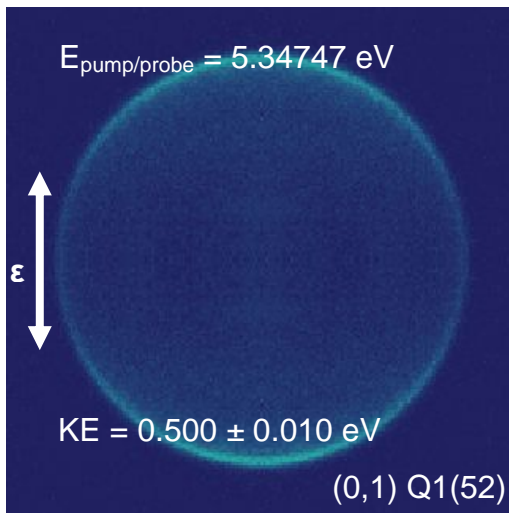
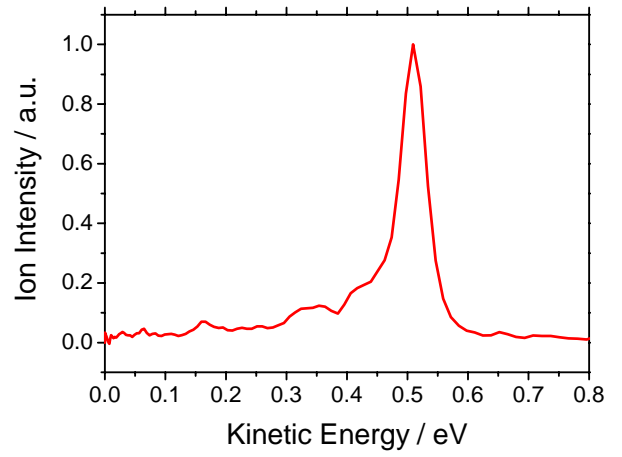
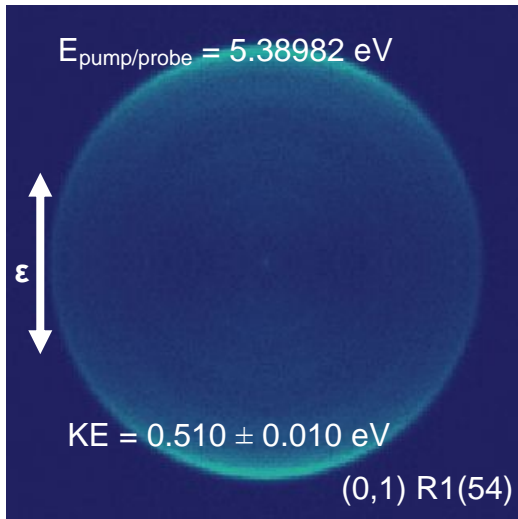
(b)



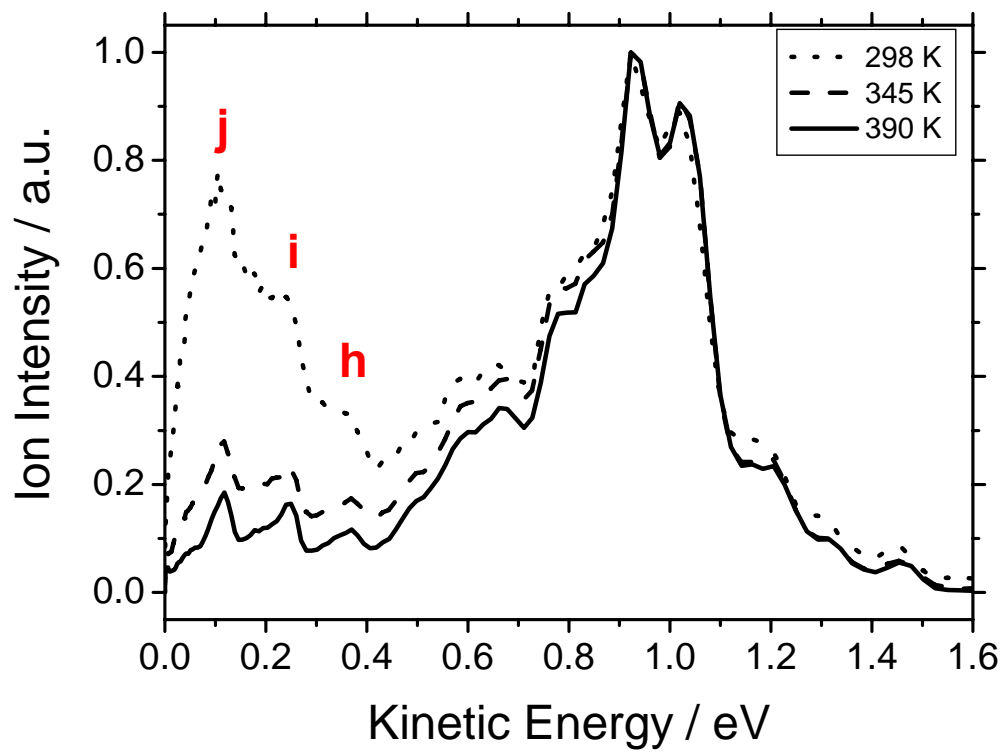
(c)



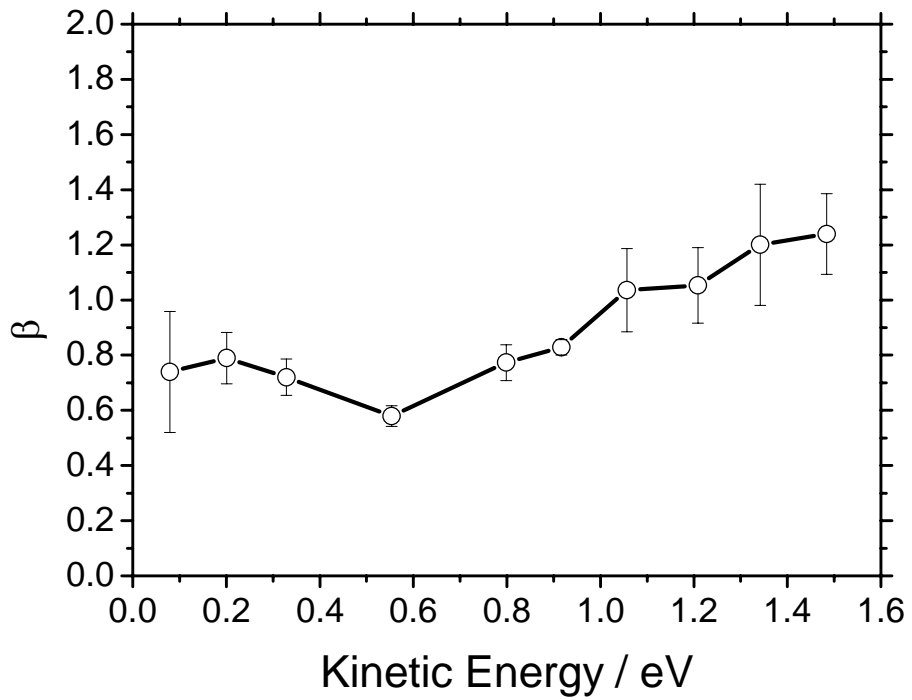
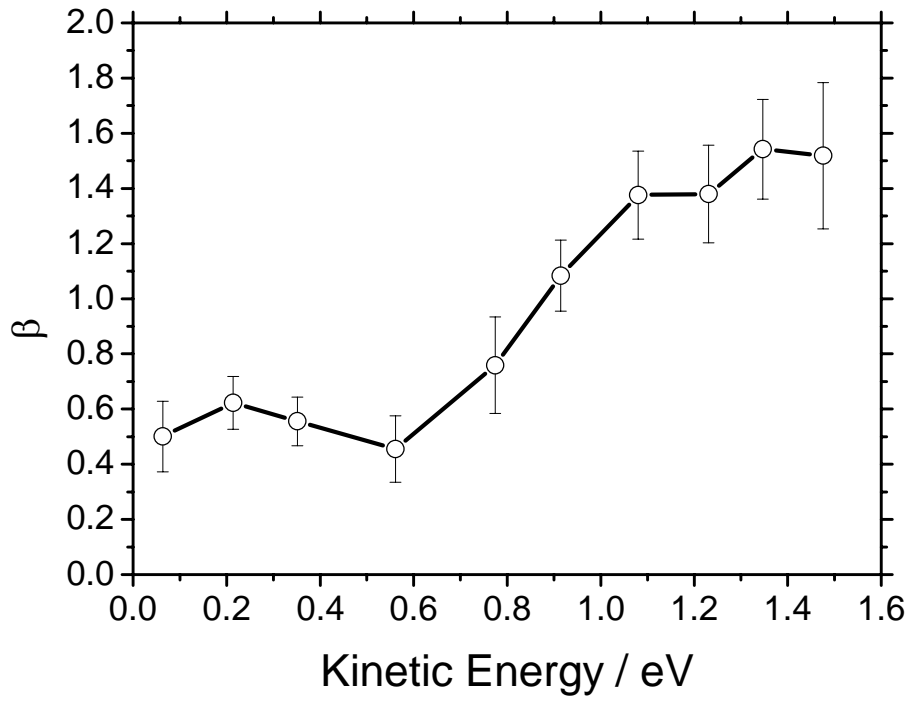
Wilkinson & Whitaker Figure 3



Wilkinson & Whitaker Figure 4



Wilkinson & Whitaker Figure 5



Wilkinson & Whitaker Figure 6